nature biomedical engineering

ARTICLES

https://doi.org/10.1038/s41551-022-00903-4

Check for updates

Glucosylated nanoparticles for the oral delivery of antibiotics to the proximal small intestine protect mice from gut dysbiosis

Guorong Zhang[1,2,3,8], Qin Wang[1,2,3,8], Wanyin Tao[1,2,3,8], Wei Jiang[1,2,3], Eran Elinav[4,5], Yucai Wang[1,2,3,6] ✉ and Shu Zhu[1,2,3,6,7] ✉

Orally delivered antibiotics can reach the caecum and colon, and induce gut dysbiosis. Here we show that the encapsulation of antibiotics in orally administered positively charged polymeric nanoparticles with a glucosylated surface enhances absorption by the proximal small intestine through specific interactions of glucose and the abundantly expressed sodium-dependent glucose transporter 1. This improves bioavailability of the antibiotics, and limits their exposure to flora in the large intestine and their accumulation in caecal and faecal contents. Compared with the standard administration of the same antibiotics, the oral administration of nanoparticle-encapsulated ampicillin, chloramphenicol or vancomycin in mice with bacterial infections in the lungs effectively eliminated the infections, decreased adverse effects on the intestinal microbiota by protecting the animals from dysbiosis-associated metabolic syndromes and from opportunistic pathogen infections, and reduced the accumulation of known antibiotic-resistance genes in commensal bacteria. Glucosylated nanocarriers may be suitable for the oral delivery of other drugs causing gut dysbiosis.

Oral antibiotics (Abx) are the most frequent and effective medical treatment for bacterial infections. However, during such treatment, the non-absorbed portion of orally administered antibiotics may reach the caecum and colon where they can induce substantial perturbations of the human microbiota[1,2]. The mutualistic microbes' residence in the human intestinal tract is known to impact numerous physiological processes and aids in the regulation of immune and metabolic homoeostasis. Thus, antibiotic exposure can alter basic physiological homoeostasis[3–5] or even contribute to chronic diseases, such as allergies or obesity[6–8]. Furthermore, excessive antibiotic use fosters the emergence of resistant strains, and human microbiota that have been repeatedly exposed to antibiotics represent a reservoir of antibiotic-resistant genes, which are known to contribute to the increasing difficulty in controlling bacterial infections in the clinic[9,10]. Therefore, it is of paramount importance to optimize the use of antibiotics by minimizing their collateral adverse effects on gut microbiota.

Previous attempts to alter antibiotics regimens and protect the microbiota while preserving anti-pathogenic efficacy include the oral co-administration of β-lactamases, which prevented some deleterious impacts of parenteral β-lactams on microbiota[11,12]. Other approaches include the addition of non-specific absorbents, such as activated charcoal, which upon delivery to the ileum or colon result in decreased faecal concentrations of orally administered antibiotics without affecting their plasma pharmacokinetics[13,14]. Systemic administration routes for antibiotics, such as intravenous injection, offer relative benefits in protecting gut microbiota[15]; however, they are not suitable for use in non-hospital settings. Thus, alternative methods are in urgent demand to manage the dysbiosis caused by orally administrated antibiotics.

The abundance and composition of gut microbiota vary across different regions of the intestine. The number of bacteria generally ranges from ~10^5 ml^{-1} in the upper small intestine to 10^{12} ml^{-1} in the colon[16]. Here we show that the effective absorption of antibiotics in the proximal small intestine limits their exposure to flora in the large intestine, and their accumulation in caecal and faecal contents. After discovering that the sodium-dependent glucose transporter 1 (SGLT1) is highly expressed in the proximal small intestine, we designed positive glucosylated nanoparticles (PGNPs) for efficient absorption by the proximal small intestine by exploiting glucose–glucose-transporter binding, thus avoiding side effects on the microbiota in the colon (Extended Data Fig. 1). The cationic and glucosylated surface enables the glucosylated nanoparticles to target the intestinal mucus layer and epithelial cells in the proximal small intestine, respectively, thus facilitating the targeted absorption of antibiotics. Treatment of animals with the glucosylated antibiotic-encapsulating nanoparticles markedly decreased adverse effects on intestinal microbiota, lowered both dysbiosis-associated opportunistic pathogen infection and metabolic syndrome, and reduced the accumulation of known antibiotic-resistance genes in commensal bacteria.

Results

SGLT1 and glucose transporter type 2 (GLUT2) are highly expressed in the small intestine, but not in the colon. Glucose uptake at the apical side of intestinal epithelial cells is mediated

[1]Department of Digestive Disease and Intelligent Nanomedicine Institute, The First Affiliated Hospital of USTC, Division of Life Sciences and Medicine, University of Science and Technology of China, Hefei, China. [2]Institute of Immunology, University of Science and Technology of China, Hefei, China. [3]The CAS Key Laboratory of Innate Immunity and Chronic Disease, School of Basic Medical Sciences, Division of Life Sciences and Medicine, University of Science and Technology of China, Hefei, China. [4]Systems Immunology Department, Weizmann Institute of Science, Rehovot, Israel. [5]Microbiome & Cancer Division, DKFZ, Heidelberg, Germany. [6]Institute of Health and Medicine, Hefei Comprehensive National Science Center, Hefei, China. [7]School of Data Science, University of Science and Technology of China, Hefei, China. [8]These authors contributed equally: Guorong Zhang, Qin Wang, Wanyin Tao. ✉e-mail: yucaiwang@ustc.edu.cn; zhushu@ustc.edu.cn

by glucose transporters[17]. However, the spatial distribution of glucose transporters along the intestine remains unknown. Using RNA sequencing, we found that the expression of *SGLT1* in the small intestine (reads per kilobase million, RPKM 700~1,000) is 19-fold higher than that in the colon (RPKM ~49). Moreover, *GLUT2*, *GLUT5* and *GLUT7* exhibit higher expression levels in the small intestine than in the colon. Among these transporters, *SGLT1* and *GLUT2* are known to mediate intestinal glucose absorption. In contrast, low levels of *SGLT2*, *GLUT3*, *GLUT4*, *GLUT6* and *GLUT8* were detected in both the small intestine and colon (Fig. 1a). Simultaneously, we detected the gene expression of SGLT1 in the jejunum, ileum and large intestine in human tissues by real-time PCR. In agreement with the mouse data, the results show that SGLT1 is highly expressed in the small intestine, but not in the colon (Supplementary Fig. 1). Thus, we propose that the higher distribution of *SGLT1* and *GLUT2* in the small intestine than in the colon might enable glucose transporter-mediated targeting of nanoparticles in the proximal small intestine.

Glucosylated nanocarriers promote absorption specifically at proximal small intestine. Inspired by the above observation, we designed nanocarriers that target the proximal small intestine by exploiting the glucose–glucose transporter binding capacity. Moreover, the inner surface of the intestine is covered by a thick mucus layer, which can reduce the accessibility of nanocarriers to epithelial cells[18]. Therefore, we further introduced a positively charged lipid moiety into the nanocarriers to promote their penetration through the mucus layers. Specifically, we designed and prepared four nanoparticles—NPs, GNPs (glucosylated nanoparticles), PNPs (positive nanoparticles) and PGNPs (positive glucosylated nanoparticles) (Fig. 1b, and Supplementary Figs. 2 and 3). Dynamic light scattering (DLS) measurements and transmission electron microscopy (TEM) observations show that these nanoparticles are monodispersed, with similar diameters of approximately 100 nm. The surface zeta potentials of NPs, GNPs, PNPs and PGNPs are approximately −9, −14, 18 and 18 mV, respectively (Fig. 1c,d).

To facilitate visualization of the distribution of nanoparticles in vivo, we encapsulated a fluorescent dye (1,1'-dioctadecyl-3,3,3',3'-tetramethylindodicarbocyanine, 4−chlorobenzenesulfonate salt, DiD) into the nanoparticles (Supplementary Fig. 4). All the nanoparticles were stable without evident DiD release in simulated gastric and intestinal fluids within 12 h (Supplementary Fig. 4). C57BL/6 mice were orally administered with DiD-loaded nanoparticles, and the intestine was fluorescently imaged using an in vivo imaging system (IVIS). PGNPs-administered mice reached a peak intestinal absorption 1 h after administration, which was faster than the free dye-administered group (Fig. 1e–g). The signal intensity for PGNPs was higher in the small intestine and substantially lower in the large intestine, as compared with the free dye or the other dye-labelled nanoparticles (Fig. 1f–h and Supplementary Fig. 5). We also used hydrophilic dye Rhodamine B (RhoB)-conjugated poly(lactic-co-glycolic acid) (PLGA) polymers to label the nanoparticles. We found that the distribution of the PLGA-RhoB-labelled nanoparticles in the intestinal tract was consistent with the distribution of DiD-labelled nanoparticles (Supplementary Fig. 6). We also studied the micro-distribution of nanoparticles in the proximal small intestine at 1 h post administration. The results show that the uptake of PGNPs by intestinal epithelial cells is higher than that of other NPs (Supplementary Fig. 7). Immunofluorescent staining of intestine sections shows that PGNPs are co-localized with SGLT1 in proximal small intestinal epithelium cells. Moreover, PGNPs' fluorescence signal intensity is positively correlated with SGLT1 expression (Supplementary Fig. 8). Notably, decreasing the density of glucose ligands on PGNPs hinders their absorption by the proximal small intestine (Supplementary Fig. 9). The above results collectively indicate that absorption can be mediated by specific interactions between glucose on PGNPs and SGLT1 in the small intestine.

To further demonstrate this, we used chemical inhibitors, phlorizin or mizagliflozin, to block SGLT1 function in vivo, which resulted in a notable reduction in the absorption of dye-labelled PGNPs in the small intestine. In contrast, no such reduction in the absorption of PNPs was observed upon treatment with SGLT1 inhibitors (Fig. 1i–l and Supplementary Fig. 10). Meanwhile, blocking GLUT2 with the chemical inhibitor phloretin had no effect on the uptake of PNPs or PGNPs into intestinal cells (Fig. 1i–l). Moreover, upon over-expressing SGLT1 in the 293T cell line, we observed an increased influx of dye-labelled PGNPs, but not PNPs, into cultured cells (Fig. 1m,n). Furthermore, PGNPs were highly co-localized with SGLT1 during internalization, as observed under the microscope (Extended Data Fig. 2). Further, we found that SGLT1-mediated cellular uptake in HEK 239T cells was heavily dependent on the size of PGNPs, and PGNPs with a size of 120 nm entered cells more efficiently than larger nanoparticles (Supplementary Fig. 11). Collectively, these results indicate that the glycosylation functionalization of nanoparticles promotes their absorption at the proximal small intestine via the glucose transporter SGLT1 (Fig. 1o).

PGNPs reduce intestinal residues and enhance blood circulation. We assessed whether the enhanced absorption of PGNPs at the proximal small intestine could reduce intestinal residues and increase their entry into the blood stream through epithelial cell absorption. At different time points post oral administration, the amount of residual DiD-loaded PGNPs in faecal and caecal contents was quantified by the IVIS imaging system. Significantly more DiD had been absorbed in mice administered with PGNPs as compared with free dye or the other labelled nanoparticles (Fig. 2a–d).

Furthermore, we conducted immunofluorescence staining of Rab11a in both HEK293T cells and proximal small intestine tissue,

Fig. 1 | Glucosylated nanocarriers promote absorption specifically at the proximal small intestine. a, RNA-seq analysis of the expression levels of *SGLTs* (left) and *GLUTs* (right) in the small and large intestines of mice. $n = 4$ mice. **b**, Schematic showing the structure and composition of indicated nanoparticles used in this work. **c**, Size distribution and zeta potential of indicated nanoparticles determined by DLS. **d**, TEM images of indicated nanoparticles. Scale bars, 100 nm. **e**, Representative IVIS spectrum at 1 h after oral administration of free DiD or DiD-labelled NPs, GNPs, PNPs or PGNPs, in three intestine regions: proximal small intestine (SI-P), distal small intestine (SI-D) and large intestine (LI). **f**–**h**, Absorption dynamics for various nanoparticles in vivo. Quantification of IVIS images at 1 h, 4 h, 8 h and 12 h after oral administration of DiD-labelled nanoparticles in SI-P (**f**), SI-D (**g**) or LI (**h**). $n \geq 3$ mice. **i**–**l**, Analysis of glucose transporter-mediated absorption of PGNP nanoparticles in mice. Representation of IVIS images for PNPs and PGNPs in intestines after oral gavage of the SGLT1 inhibitor phlorizin or the GLUT2 inhibitor phloretin (**i**), and quantification of the fluorescence signals in SI-P (**j**), SI-D (**k**) or LI (**l**). $n \geq 4$ mice. **m**,**n**, Analysis of glucose transporter-mediated absorption of PGNP nanoparticles in cells. **m**, Confocal images of PGNPs (red) taken up by *SGLT1* or *GLUT2*-expressing HEK293T cells (green). Scale bars, 10 μm. **n**, Quantification of data in **m**. **o**, Schematic representation showing that PGNPs can be taken up and transported by intestinal epithelial cells (IECs) through SGLT1-mediated transport following oral administration. All values are expressed as mean ± s.e.m. Statistical significance was determined using two-way ANOVA with Tukey's multiple comparisons in **f**–**h**, **j** and **k**, and one-way ANOVA with Tukey's multiple comparisons in **n**. $^{*}P < 0.05$, $^{**}P < 0.01$, $^{***}P < 0.001$, $^{****}P < 0.0001$. NS, not significant. Data in **e**–**n** are representative of at least 3 independent experiments.

and found that the majority of cytoplasmic PGNPs co-localized with Rab11a, a marker of recycling endosomes that regulates the exocytosis of cellular vesicles (Extended Data Fig. 3). These data suggest that the delivery of PGNPs probably occurs through SGLT1-mediated endocytosis followed by endosome-mediated transcytosis. Blood concentrations of nanoparticles were measured using confocal laser scanning microscopy (CLSM)-based real-time visualization of the ear vasculature in mice. Observably, PGNPs-treated mice featured higher concentrations in blood compared with the other NPs (Fig. 2e,f). PGNPs with larger sizes reduced their entry into the systemic circulation through the proximal small intestine (Supplementary Fig. 12). Moreover, we also assessed the accumulation of nanoparticles in major organs 1 h after oral administration. A large amount of PGNPs were measured in the proximal small intestine (SI-P) and distal small intestine (SI-D) (Supplementary Fig. 13). In summary, these results indicate that glycosylated functionalization of nanoparticles reduces their faecal/caecal content residues and promotes their absorption in blood.

Subsequently, we examined whether PGNPs as carriers could increase the bioavailability and blood circulation of encapsulated

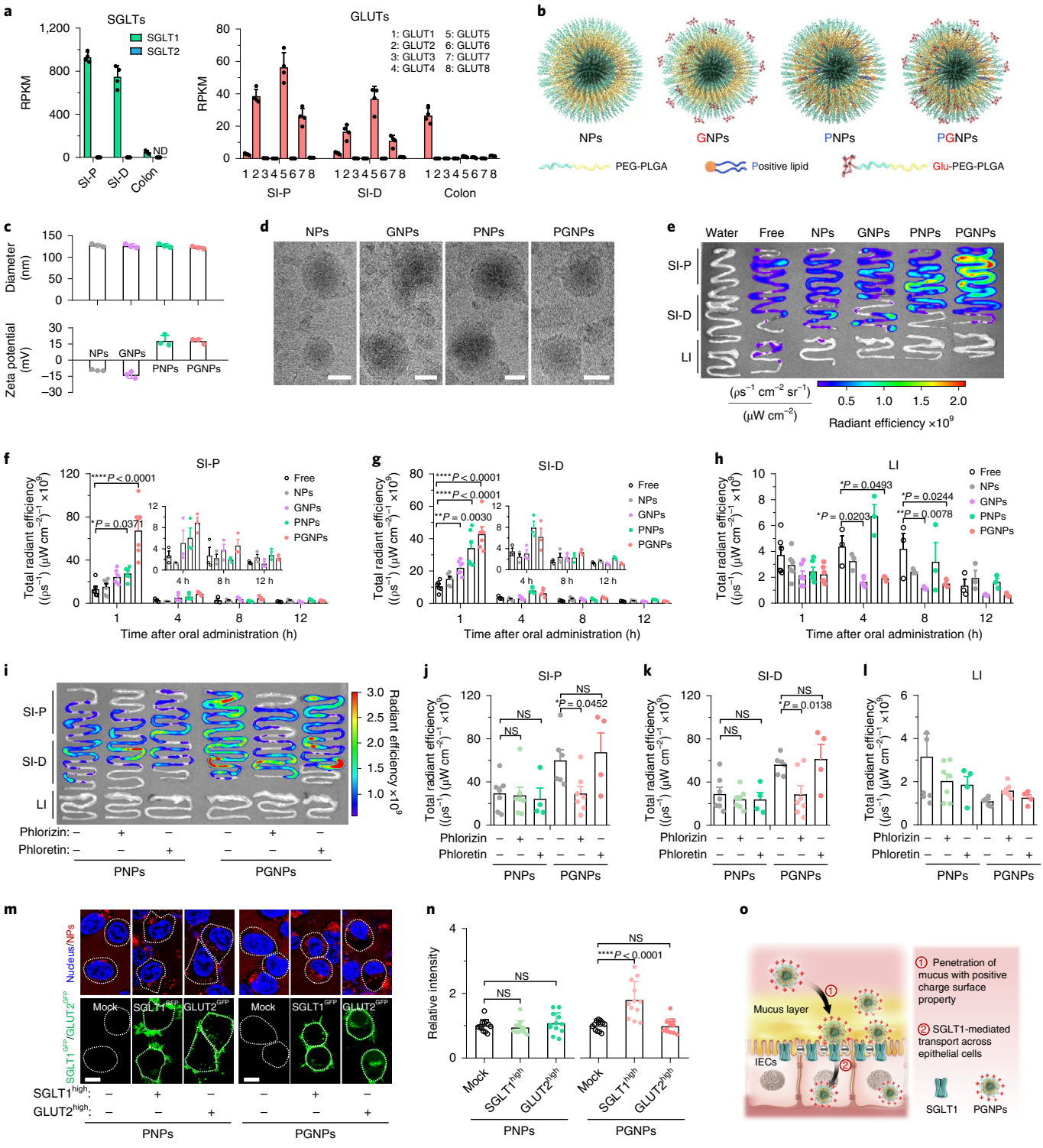

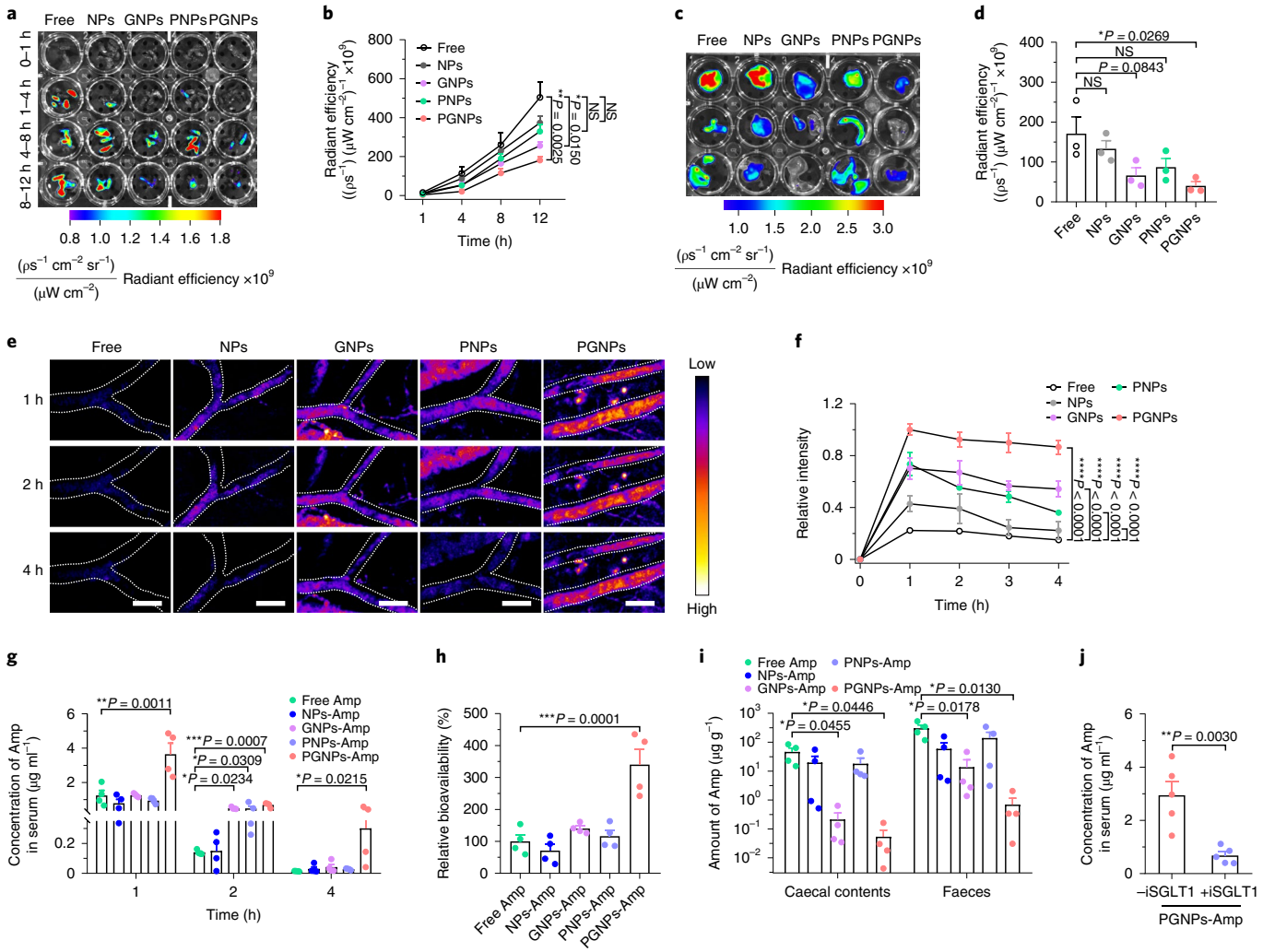

Fig. 2 | PGNPs reduce intestinal residues and enhance blood circulation. a–d, Representative images (**a**,**c**) and quantitative data (**b**,**d**) for residual nanoparticles in faecal contents at different time points (**a**,**b**), and in caecal contents at 12 h post oral administration (**c**,**d**). $n = 3$ mice. **e**, Time-lapse confocal fluorescence microscopy visualizing DiD-labelled NPs in ear vasculature of mice after oral administration. Scare bars, 100 μm. **f**, Quantification of the fluorescence intensity of nanoparticles in **e**. $n = 3$ mice. **g**, The concentration of Amp in serum following a single-dose oral administration of free Amp or Amp-loaded nanoparticles (40 mg kg^{-1}) in wild-type mice. **h**, Relative bioavailability of free Amp or Amp-loaded nanoparticles. The relative bioavailability of each group was determined from the area under the curve (AUC) of Amp-loaded nanoparticles compared to the AUC of free Amp, expressed as a percentage. **i**, The residual Amp in caecal and faecal contents from mice 4 h after oral administration of free Amp or Amp-loaded nanoparticles. $n = 4$ mice. **j**, In vivo SGLT1 inhibition study. The serum concentration of Amp in mice at 1 h after oral administration of PGNPs-Amp. Phlorizin treatment took place 1 h before administration. $n = 5$ mice. All values are expressed as mean ± s.e.m. Statistical significance was determined using one-way ANOVA with Tukey's multiple comparisons in **b**, **d**, **f**, **g** and **h**, two-way ANOVA with Tukey's multiple comparisons in **i** and two-tailed Student's *t*-test in **j**. $^*P < 0.05$, $^{**}P < 0.01$, $^{***}P < 0.001$, $^{****}P < 0.0001$.

antibiotics. Ampicillin (Amp) was used as a model antibiotic. In vitro drug release experiments indicated that Amp was released slowly from PGNPs after incubation in simulated buffers (Supplementary Fig. 14). In vivo, the concentration of Amp peaked 1 h after oral administration and subsequently decreased with time (Fig. 2g). The serum concentration of Amp for the PGNPs-Amp group was 20.9-fold higher than that of free Amp at 4 h post administration (Fig. 2g). Moreover, the bioavailability of PGNPs-Amp within the first 4 h was 2.4–4.8-fold higher than that of the other groups (Fig. 2h), indicating that Amp-loaded PGNPs exhibits prolonged retention in blood. In line with this result, the amount of Amp distributed in major organs was elevated. These data showed a distribution pattern of PGNPs-Amp indicative of enhanced absorption of Amp in small intestine and blood compared with free Amp (Supplementary Fig. 15). In addition, PGNPs delivery also prolonged the blood circulation of chloramphenicol and increased its bioavailability (Supplementary Fig. 16).

The Amp residues in the caecal and faecal contents reached 46.4 and 303.5 μg g^{-1} in free-Amp-treated mice, while the residues were 0.05 and 0.69 μg g^{-1} in PGNPs-Amp-treated mice (Fig. 2i). When using the chemical inhibitor phlorizin to block SGLT1 function in vivo, we detected a 4.3-fold reduction in serum levels (Fig. 2j) and a 2.3-fold reduction in the proximal small intestine levels of the concentration of Amp, while an increased absorption of Amp in the colon was detected in comparison with PGNPs-Amp administration alone (Supplementary Fig. 17). This suggests that the glucose transporter SGLT1 is essential for achieving spatial absorption of antibiotics into the serum.

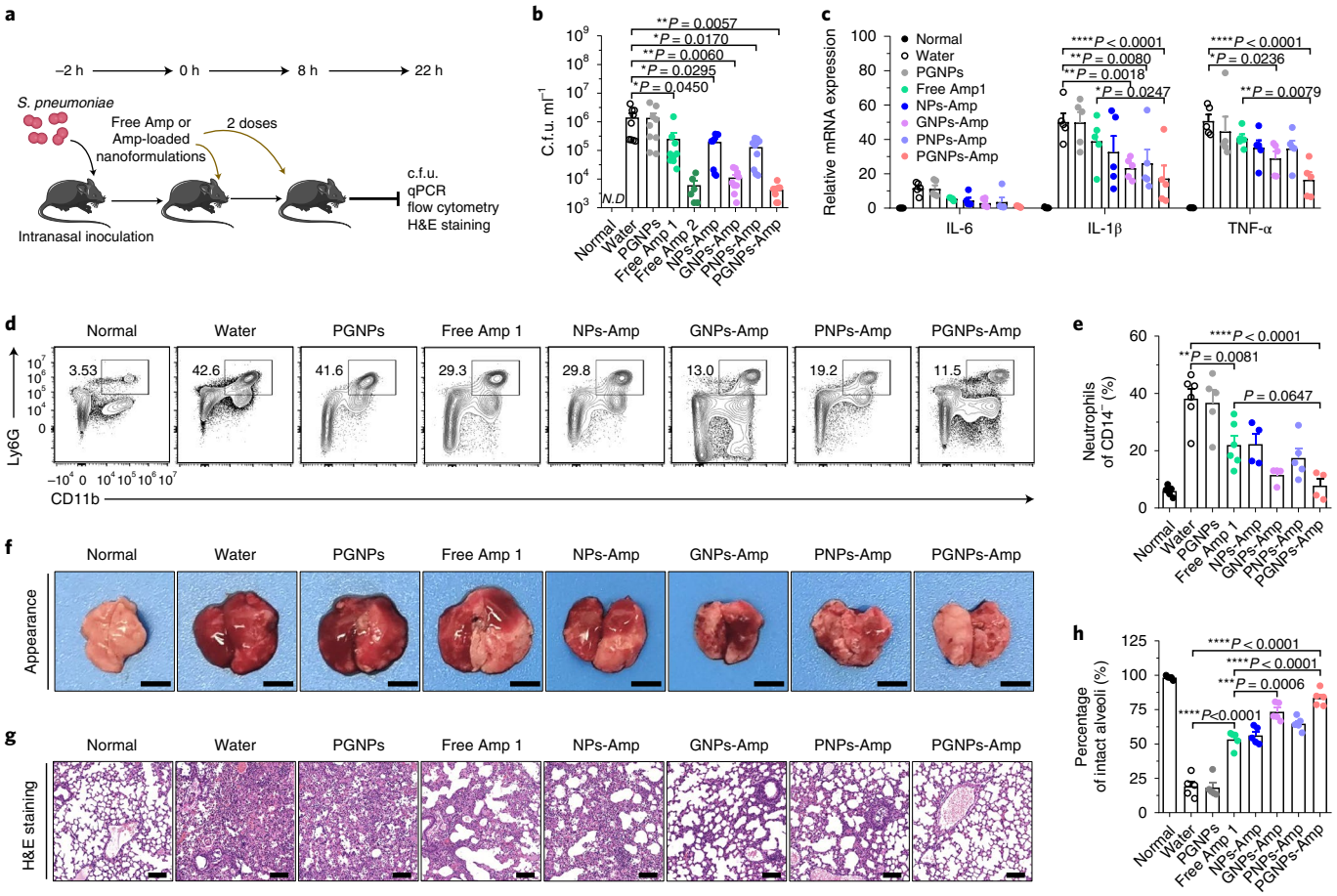

Fig. 3 | PGNPs-Abx effectively eliminates *S. pneumoniae* infection in lung. a, Schematic of the experimental design: mice received an intranasal challenge with 3×10^8 c.f.u.s of *S. pneumoniae*. Free Amp or Amp-loaded nanoparticles were orally administered to mice. Control mice did not receive antibiotic treatment. The bacterial load in lung, cytokine expression, infiltrated neutrophils and lung pathology were determined at 24 h post *S. pneumoniae* infection. **b**, Bacterial loads in the lungs at 24 h post infection. Free Amp 1 and other Amp-loaded nanoparticles (40 mg kg^{-1}), free Amp 2 (200 mg kg^{-1}). $n \geq 6$ mice. **c**, qPCR of indicated inflammatory cytokines. $n = 5$ mice. **d**, Representative flow cytometry plots of CD11b$^+$ Ly6G$^+$ CD14$^-$ neutrophils in lungs at 24 h post infection. **e**, Quantification of **d**. $n \geq 4$ mice. **f**, The appearance of lungs at 24 h post infection. Scale bars, 5 mm. **g**, Haematoxylin and eosin (H&E) staining of lungs at 24 h post infection. Scale bars, 100 μm. **h**, Quantification of intact alveoli in **g**. $n = 5$ mice. All values are expressed as mean ± s.e.m. Statistical significance was determined using one-way ANOVA with Tukey's multiple comparisons in **b**, **e** and **h**, and two-way ANOVA with Tukey's multiple comparisons in **c**. $^*P < 0.05$, $^{**}P < 0.01$, $^{***}P < 0.001$, $^{****}P < 0.0001$. ND, not detected. Data in **b** are representative of 3 independent experiments.

PGNPs-Abx effectively eliminates *Streptococcus pneumoniae* infection in lung. To test whether the nanocarrier delivery system affects the anti-bacterial efficacy of antibiotics, we evaluated the anti-bacterial efficacy of various formulations of Amp-loaded nanoparticles vs free Amp in a mouse model of lung infection (pneumococcal pneumonia) mediated by *S. pneumoniae*, one of the most frequent causal pathogens for respiratory tract infections[19] (Fig. 3a). In comparison with the same dose of free Amp, which modestly reduced bacterial loads in the lung, PGNPs-Amp cleared pulmonary bacteria with a significantly higher efficiency. The efficacy of PGNPs-Amp was comparable to that of a 5-fold higher dose of free-Amp treatment (Fig. 3b). GNPs-Amp also showed better anti-bacterial efficacy than free Amp (Fig. 3b). In contrast, NPs and PNPs did not increase the anti-bacterial efficacy in comparison with the free Amp (Fig. 3b). These results are consistent with the relatively high distributions of GNPs-Amp and PGNPs-Amp in lung (Supplementary Fig. 15).

The measurement of inflammatory cytokines and neutrophils in lungs shows substantially reduced inflammation in PGNPs-Amp or GNPs-Amp groups compared with mice treated with free Amp and other Amp-loaded nanoparticles (Fig. 3c–e and Supplementary Fig. 18). Moreover, pulmonary pathological and histological analyses showed diminished inflammation and pathology in both free Amp and other NPs-Amp groups compared with vehicle-treated mice (Fig. 3f–h), Notably, lower inflammation and attenuated tissue damage were observed in PGNPs-Amp or GNPs-Amp-treated animals compared with free Amp and other NPs-Amp-treated animals (Fig. 3f–h).

We used the bacteremia model to further characterize anti-bacterial efficacies of antibiotics-loaded PGNPs. Mice were challenged intravenously with a defined dose of the gram-positive bacterium *Listeria monocytogenes* and subsequently treated with free Amp and PGNPs-Amp at pre-determined time points (Extended Data Fig. 4a). The appearance of liver and spleen indicated diminished inflammation in both free Amp and PGNPs-Amp groups in comparison with control groups, with significantly reduced inflammation in the PGNPs-Amp group (Extended Data Fig. 4b). The pathogen load was assessed by measuring c.f.u.s in the peripheral blood, liver and spleen at 24 h after infection. Similar to what we observed in the lung infection model, PGNPs-Amp-treated mice cleared *L. monocytogenes* more efficiently than free-Amp-treated mice (Extended Data Fig. 4c–e). In summary, these results suggest

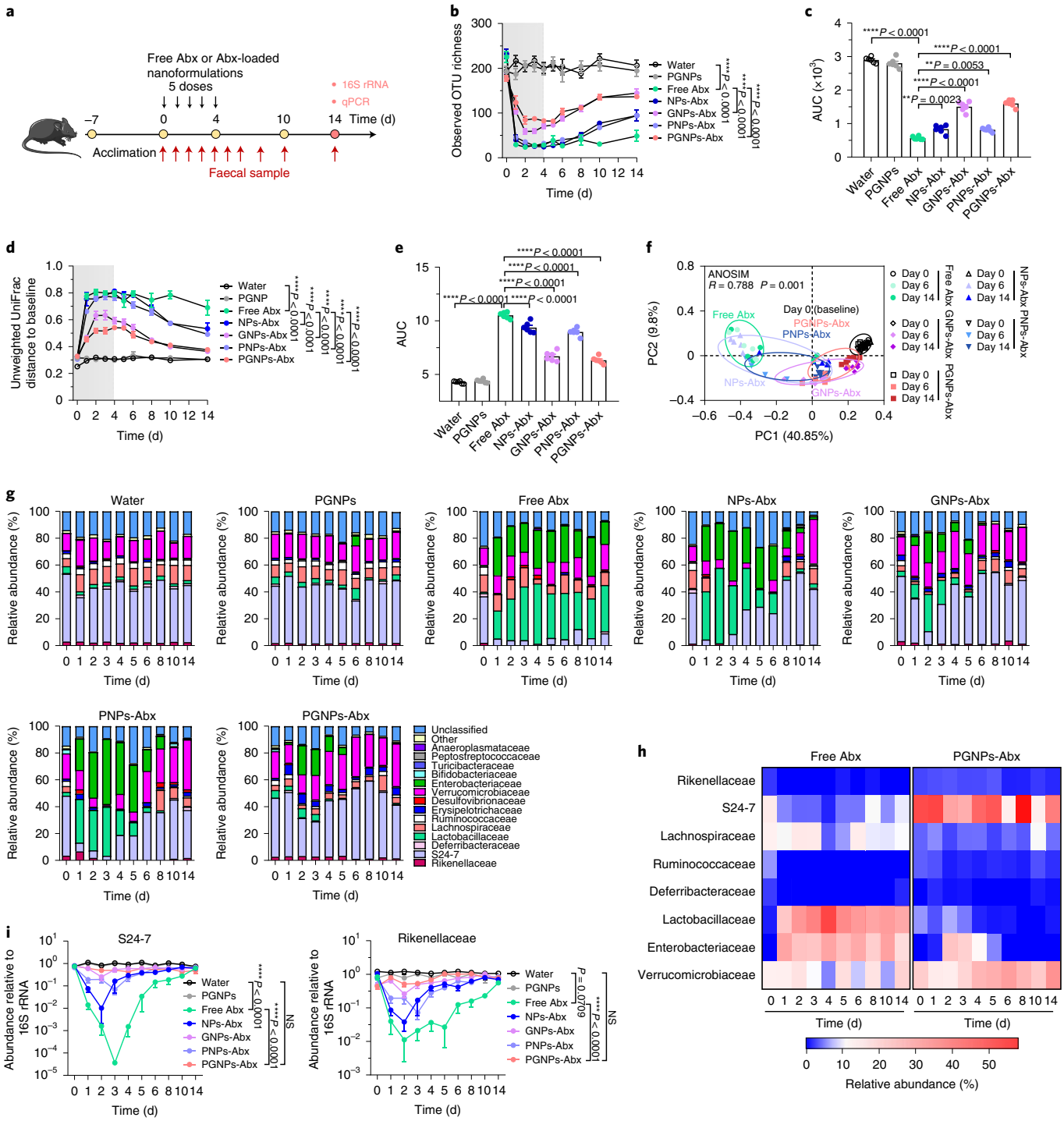

Fig. 4 | PGNPs delivery prevents antibiotic-induced dysbiosis. a, Schematic showing the experimental design: C57BL/6 mice were orally administered with free antibiotics or nanoparticles encapsulating ampicillin (20 mg kg^{-1}) and vancomycin (20 mg kg^{-1}) for 5 doses in 5 d. Control mice had no antibiotic exposure. Faecal samples were collected longitudinally at multiple time points for 16S rRNA sequencing and qPCR. **b**, Estimation of microbial community α-diversity (observed OTU richness) in different groups. The shaded area represents the free Abx or Abx-loaded nanoformulations treatment. **c**, Area under the α-diversity curve from day 0 of antibiotics treatment. **d**, Unweighted UniFrac distances to baseline in faeces between free antibiotics and antibiotics-loaded nanoparticles-treated mice. **e**, AUC of 16S rRNA-based unweighted UniFrac distances. **f**, PCA plot generated from an unweighted UniFrac distance matrix displaying the distinct clustering pattern of the intestinal bacteria community for mice of the different treatment groups. The circles refer to the confidence degree and represent the distribution of different samples in the same group. **g**, Relative abundance data for gut microbiota (family-level taxonomy) are presented as a percentage of the total detected sequences. **h**, Heat map of the relative abundance of family-level taxa for each group. $n \geq 4$ mice. **i**, Relative abundance of select taxa (S24-7 and Rikenellaceae) assessed on the basis of qPCR analysis of faecal samples. $n \geq 3$ mice. All values are expressed as mean ± s.e.m. Statistical significance was determined using two-way ANOVA with Tukey's multiple comparisons in **b**, **d** and **i**, or one-way ANOVA with Tukey's multiple comparisons in **c** and **e**. $^{*}P < 0.05$, $^{**}P < 0.01$, $^{***}P < 0.001$, $^{****}P < 0.0001$. Data in **b**–**h** are representative of 4 independent experiments, the experiment in **i** was repeated 3 times.

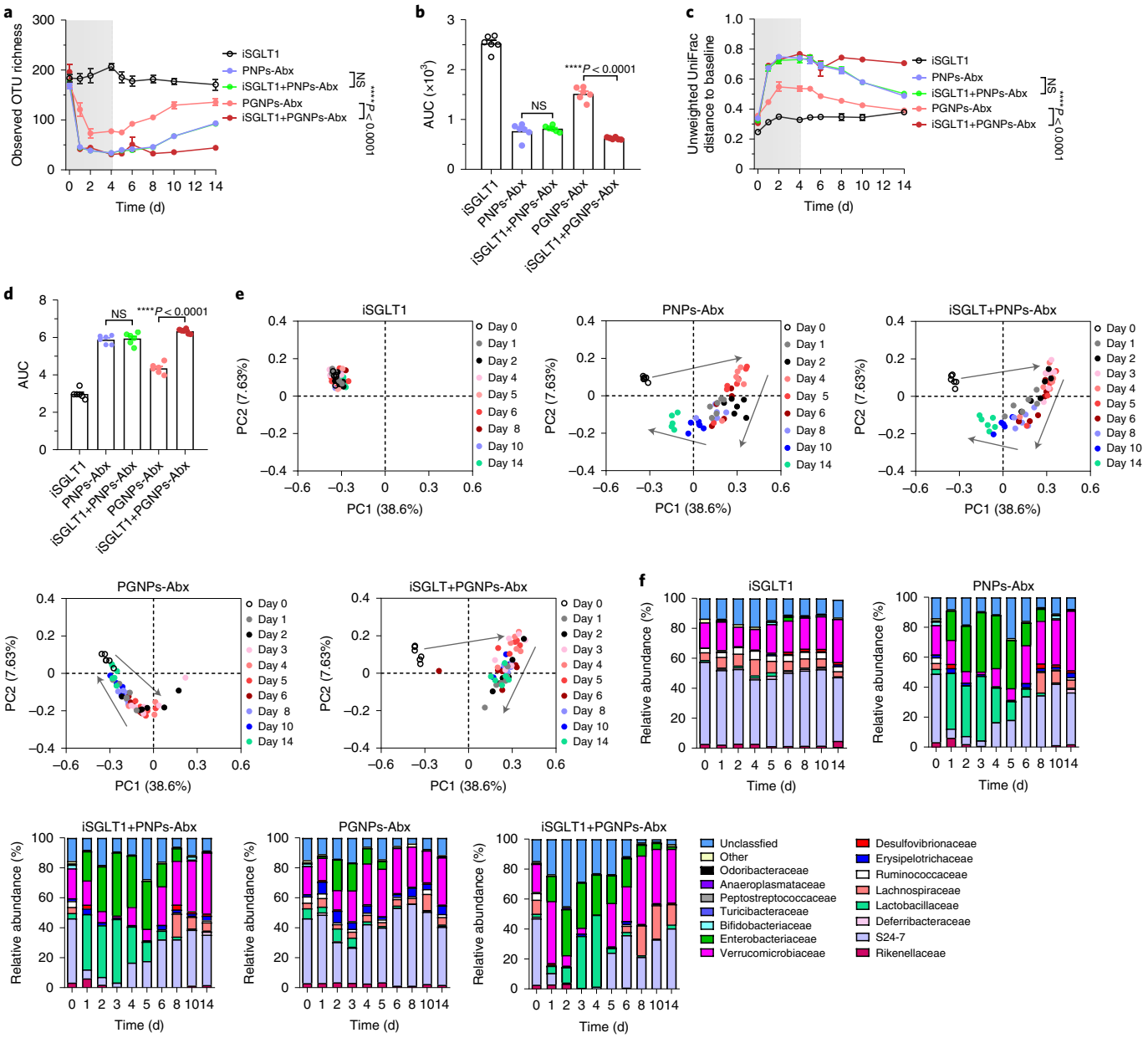

Fig. 5 | The SGLT1 inhibitor eliminates the protective effect of PGNPs-Abx. C57BL/6 mice were first orally gavaged with the SGLT1 inhibitor phlorizin at 50 mg kg^{-1} body weight for 1 h, followed by oral administration of ampicillin (20 mg kg^{-1}) and vancomycin (20 mg kg^{-1})-loaded PNPs or PGNPs for 5 d. Control mice iSGLT1 group had no antibiotic exposure. Faecal samples were collected longitudinally at multiple time points for 16S rRNA sequencing. **a**, The microbial community α-diversity (observed OTU richness) in faecal samples from mice with indicated treatments. The shaded area represents the SGLT1 inhibitor phlorizin or Abx-loaded nanoformulations with or without phlorizin treatment. **b**, Area under the α-diversity curve for data in **a**. **c**, Unweighted UniFrac distances to baseline in faecal samples from mice with indicated treatments. **d**, AUC for data in **c**. **e**, PCA plot generated from an unweighted UniFrac distance matrix displaying the distinct clustering pattern of the intestinal bacterial community in faecal samples from mice with indicated treatments. **f**, Relative abundance of gut microbiota in different families at indicated treatments, presented as a percentage of the total detected sequences. $n \geq 5$ mice. All values are expressed as mean ± s.e.m. Statistical significance was determined using two-way ANOVA in **a** and **c**, and one-way ANOVA with Tukey's multiple comparisons in **b** and **d**. $^*P < 0.05$, $^{**}P < 0.01$, $^{***}P < 0.001$, $^{****}P < 0.0001$. Data in **a**–**f** are representative of 2 independent experiments.

that PGNPs-Amp exhibits enhanced efficacy in terms of clearance of bacterial pathogens.

We further evaluated the safety of PGNPs. The serum biochemical analysis and histological analysis of multiple organs after PGNPs administration for 10 d showed no evident differences in comparison with water administration (Supplementary Fig. 19). Accordingly, these results demonstrated that antibiotics delivery based on our glycosylated nanocarrier route can outperform free antibiotics for the treatment of systemic infection.

PGNPs delivery prevents antibiotics-driven dysbiosis. One possible advantage of the efficient absorption of orally administered PGNPs at the proximal small intestine may be a reduced perturbation to gut microbiota. Notably, antibiotics-induced dysbiosis may exert a substantial impact on the abundance of 30% of bacterial taxa in the gut community, resulting in rapid and considerable reductions in taxonomic richness, diversity and evenness[20]. Importantly, indigenous microbiome reconstitution following antibiotics treatment may be highly variable[21], thereby exposing treated patients,

and especially children, to an increased risk of development of dysbiosis-related disorders[22]. We therefore tested the impacts of freely administered ampicillin and vancomycin vs identical doses of various antibiotics-loaded nanoparticles on the gut microbiota at several time points (Fig. 4a).

As expected, 16S ribosomal RNA sequencing results showed that the free Abx treatment resulted in a substantial reduction in stool α-diversity (Fig. 4b,c) and general disruption of the faecal bacterial community structure, based on the unweighted UniFrac distance to the baseline (Fig. 4d,e). Notably, PGNPs-Abx and GNPs-Abx led to lower interruption to the gut microbiota, as well as a more rapid restoration of faecal bacterial richness and community structure compared with both NPs-Abx and PNPs-Abx groups (Fig. 4b–e). The analysis of UniFrac distances to infer the kinetics for faecal composition restoration also reveals that the faecal bacterial composition in the PGNPs-Abx or GNPs-Abx treatments was restored to baseline levels faster than in the free Abx or other NPs-Abx treatments (Fig. 4f and Extended Data Fig. 5).

Further analysis at the family level shows that the free Abx treatment resulted in a decrease in bacterial families, including Ruminococcaceae, Rikenellaceae and S24-7, and causes an increase in Enterobacteriaceae (Fig. 4g,h). In contrast, the PGNPs-Abx treatment had little impact on the family-level composition of faecal microbiota (Fig. 4g,h). To verify our 16S rRNA sequencing results, we performed qPCR with primers specific to S24-7 and Rikenellaceae taxa. Consistently, we found that the relative abundance of both S24-7 and Rikenellaceae was significantly decreased in faeces of the free Abx group, but not in the PGNPs-Abx group. Among the other three treatment groups, NPs-Abx exhibits the most notable change, followed by PNPs-Abx and GNPs-Abx (Fig. 4i). Thus, the spontaneous recovery of microbiota following oral broad-spectrum antibiotics or antibiotics-loaded nanoparticles shows that glycosylated nanoparticles delivery largely protects against antibiotics-induced microbiota alterations, including changes in bacterial richness, diversity and composition, and that oral administration of PGNPs-Abx is associated with a lower degree of long-term dysbiosis.

Apart from faecal microbiota, we examined microbiota alterations in the small intestine by 16S rRNA gene sequencing. Consistent with the findings in faecal samples, the number of observed species and the microbial community composition in the proximal and distal small intestinal contents were barely changed in the PGNPs-Abx treatment group, while the free Abx treatment resulted in a substantial reduction and great disturbance (Extended Data Fig. 6a,b,d,e). A comparison of the antibiotics-induced taxonomic changes in small intestinal contents indicated that three taxa—Erysipelotrichaceae, Lachnospiraceae and S24-7—notably decreased in the free Abx group, but not in the PGNPs-Abx group (Extended Data Fig. 6c,f). Thus, PGNPs delivery also prevents antibiotics-induced dysbiosis in the small intestine.

SGLT1 inhibitor eliminates the protective effect of PGNPs-Abx. In our rational design, we decorated the nanocarriers with glucose and hypothesized that SGLT1-mediated endocytosis is important for the absorption of PGNPs. To test whether the protection of PGNPs against antibiotics-induced dysbiosis relies on SGLT1, we used phlorizin, an SGLT1 inhibitor (iSGLT1), to investigate the influence of PGNPs-Abx on the gut microbiome. In mice pretreated with phlorizin, we detected a significant reduction in bacterial diversity and a large disturbance in the bacterial composition in PGNPs-Abx co-administered with the inhibitor compared with PGNPs-Abx without the inhibitor (Fig. 5a–d). No such difference was observed between PNPs-Abx and PNPs-Abx co-administered with iSGLT1 (Fig. 5a–d). We further assessed microbiota recovery dynamics by unweighted UniFrac analysis. On the basis of UniFrac distances, while mice treated with only PGNPs-Abx showed a mild disturbance of microbiota and a rapid recovery, mice treated with PGNPs-Abx together with iSGLT1 showed a large disturbance and a slow recovery (Fig. 5e). However, mice treated with both PNPs-Abx alone and PNPs-Abx with iSGLT1 showed large disturbances and slow recoveries (Fig. 5e). Consistently, the families S24-7, Ruminococcaceae and Rikenellaceae were not altered in PGNPs-Abx-treated mice, whereas they decreased substantially in mice treated with PGNPs-Abx and iSGLT1 (Fig. 5f). No such difference was observed between PNPs-Abx and PNPs-Abx co-administered with iSGLT1 (Fig. 5f). Notably, oral administration with iSGLT1 for only 14 d had no effect on the gut microbiota (Fig. 5a–f). Collectively, these data indicate that PGNPs delivery protects the mice from antibiotics-induced disturbance of microbiota, owing to the target absorption of nanoparticles by the SGLT1 transporter in the proximal small intestine.

PGNPs delivery of antibiotics ameliorates dysbiosis-associated obesity. Recent studies support the notion that gut microbiota may modulate host metabolism, including energy homoeostasis and adiposity[7,8]. Several metabolic disorders, such as obesity, fatty liver disease and type 2 diabetes mellitus have been linked to gut microbiota dysbiosis[1], and obesity-associated microbiota have been suggested to feature an increased capacity to harvest energy from the diet[23]. To evaluate the potential impact of antibiotics-loaded nanoparticle on the antibiotic-associated metabolic syndrome, we employed the high-fat diet (HFD)-induced obesity murine model (Fig. 6a).

Treatment with a low dose of ampicillin and vancomycin resulted in an increased HFD-induced accumulation of body mass and fat mass (Fig. 6b,e). In contrast, oral administration of PGNPs-Abx was associated with a milder increase in the HFD-induced accumulation of body mass and fat mass compared with free Abx or other NPs-Abx groups (Fig. 6b,e). Similarly, the administration of free Abx resulted in altered glucose tolerance and increased HFD-induced cholesterol levels in the liver and serum (Fig. 6c,d,f). In contrast, PGNPs-Abx administration led to only a marginal change in the glucose tolerance and antibiotics-induced cholesterol

Fig. 6 | The PGNP-mediated delivery of antibiotics ameliorates dysbiosis-associated obesity. a, Schematic showing the experimental design: 3-week-old C57BL/6J male mice were administered with free antibiotics or antibiotics-loaded nanoparticles (ampicillin and vancomycin at 20 mg kg^{-1} body weight) for 5 successive days. Control mice had no antibiotics exposure. All mice received high-fat diet (HFD) treatment from the age of 7 weeks. **b**, Body weight changes in each group were monitored weekly. **c**, IPGTT for mice in **a**. **d**, The AUC of **c**. **e**, The total, visceral and subcutaneous (SubQ) fat masses were measured at the end of the HFD treatment. **f**, Serum and liver cholesterol levels at the end of the HFD treatment. **g**,**h**, Hepatic histopathology, representative H&E-stained sections (**g**) and Steatosis scores (**h**). Scale bars, 50 μm for top panels, 25 μm for bottom panels (enlarged view of dashed squares in top panels). $n = 5$ mice. **i**, Donor mice were given water, PGNPs, free Abx or PGNPs-Abx daily for 5 d. Faecal pellets were collected for FMT. Faecal bacteria were transplanted into recipient mice after Abx treatment, followed by HFD feeding to induce obesity. PO, per os (orally). **j**, Body weight changes in each group were monitored weekly. **k**, IPGTT for mice in **i**. **l**, The AUC of **k**. **m**, The total, visceral and subcutaneous fat masses were measured at the end of the HFD treatment. **n**,**o**, Hepatic histopathology, representative H&E-stained sections (**n**) and Steatosis scores (**o**). Scale bars, 50 μm for top panels, 25 μm for bottom panels (enlarged view of dashed squares in top panels). $n = 5$ mice. All values are expressed as mean ± s.e.m. Statistical significance was determined using two-way ANOVA with Tukey's multiple comparisons in **b**, **c**, **f**, **j**, **k** and **m**, or one-way ANOVA with Tukey's multiple comparisons in **d**, **e**, **h**, **n** and **o**. $^{*}P < 0.05$, $^{**}P < 0.01$, $^{***}P < 0.001$, $^{****}P < 0.0001$.

levels, compared with free Abx or other NPs-Abx groups (Fig. 6c,d,f). Furthermore, a milder liver steatosis was observed upon PGNPs-Abx administration compared with free Abx and other NPs-Abx groups (Fig. 6g,h).

We further monitored the microbiota alterations after HFD treatment for 12 weeks. We found notable alterations in microbiota in free-Abx-treated mice, while a lower influence on microbiota in PGNPs-Abx-treated mice was found even after HFD treatment for 12 weeks (Extended Data Fig. 7), indicating that the free Abx treatment prevented microbiota recovery to the baseline.

To gain a mechanistic insight on how PGNPs delivery protects mice from antibiotics-induced metabolic syndromes, we measured bile acids in the faeces and endotoxin levels in the serum, which have been shown to be associated with microbial regulation of metabolic processes[24,25]. We found no difference in serum endotoxin levels after treatment with free Abx or PGNPs-Abx (Supplementary

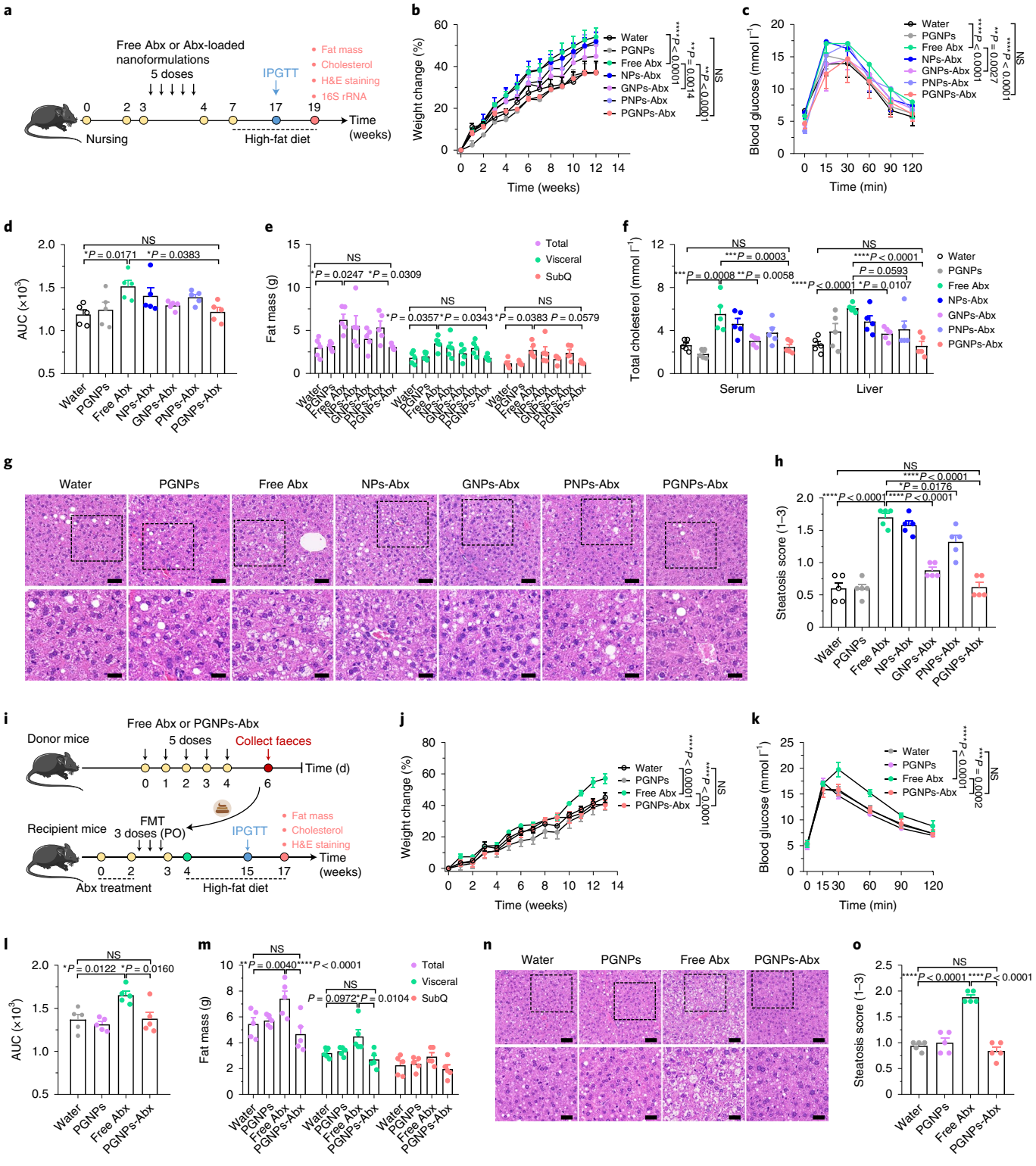

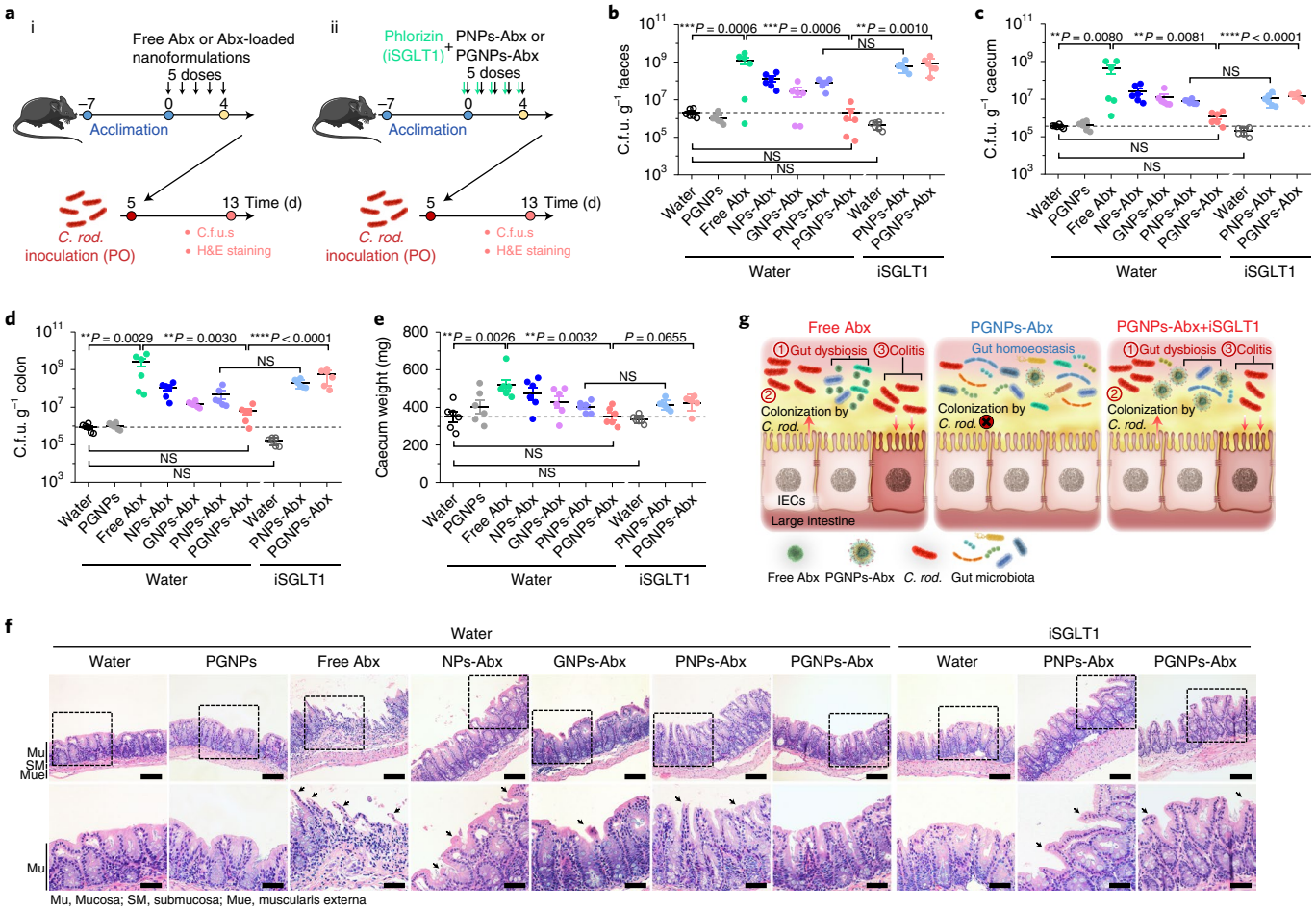

Fig. 7 | The PGNPs-mediated delivery of antibiotics via SGLT1 decreases dysbiosis-associated infection by *C. rodentium*. **a**, Schematic of the experimental design. (i) Mice were given water, PGNPs, free antibiotics or antibiotics-loaded nanoparticles (ampicillin and vancomycin, both at 20 mg kg^{-1}) daily for 5 d, and then infected intragastrically with *C. rodentium* on the following day. (ii) C57BL/6 mice were first orally gavaged with the SGLT1 inhibitor phlorizin at 50 mg kg^{-1} body weight for 1 h, followed by oral administration of PNPs-Abx or PGNPs-Abx for 5 d. Mice were then infected intragastrically with *C. rodentium* on the following day. **b**–**d**, The measurement of bacterial titres in faeces (**b**), caecal contents (**c**) and distal colon tissues (**d**). **e**, Measurement of caecum weight. **f**, Histopathology of caecal sections obtained from mice at day 8 post infection. Scale bars, 100 μm for top panels, 50 μm for bottom panels (enlarged views of dashed squares in top panels). $n = 6$ mice. **g**, Schematic diagram showing that treatment with free antibiotics decreases the diversity of the microbiota and leads to expansion of the *C. rodentium* population. Treatment with PGNPs-Abx confers little impact on microbiota. A diverse and non-disturbed microbiota confers resistance to colonization by enteric pathogens in the intestinal epithelium. Blocking of SGLT1 transporters results in alterations of microbiota by unabsorbed PGNP-Abx, leading to expansion of *C. rodentium*. All values are expressed as mean ± s.e.m. Statistical significance was determined using two-way ANOVA with Tukey's multiple comparisons in **b**–**d** and **e**. $^{*}P < 0.05$, $^{**}P < 0.01$, $^{***}P < 0.001$, $^{****}P < 0.0001$. Data in **b**–**f** are representative of 3 independent experiments.

Fig. 20); however, free Abx notably altered the levels of bile acids (Extended Data Fig. 8), many of which are reported to affect metabolism; for example, chenodeoxycholic acid (CDCA) was shown to be associated with an increase in energy expenditure[26,27]. In contrast, PGNPs delivery of antibiotics did not induce systemic alteration of bile acid levels (Extended Data Fig. 8). Thus, PGNPs delivery is beneficial for antibiotics-induced alteration of bile acids.

To investigate whether microbiota alteration or administration of free Abx or NPs-Abx caused the metabolic phenotype, we performed faecal microbiota transplantation (FMT) experiments to provide direct evidence. Donor mice were treated with free Abx or PGNPs-Abx, while control mice received no antibiotics. Faecal samples were collected from the treated mice and transferred to recipient mice. These mice were then initiated on an HFD model. The data show that mice that received gut microbiota from free-Abx-treated mice gained more weight, had higher glucose resistance, higher total cholesterol in liver and more severe liver steatosis in comparison with mice that received gut microbiota from PGNPs-Abx-treated mice (Fig. 6i–o and Extended Data Fig. 9). These results suggest that PGNPs delivery of antibiotics mitigates dysbiosis-associated metabolic alterations.

PGNPs delivery of antibiotics via SGLT1 decreases dysbiosis-associated *Citrobacter rodentium* infection. Another important adverse effect stemming from antibiotics-induced dysbiosis is an increased susceptibility to pathogenic intestinal infections. These infections result from invasion by acquired enteric pathogens or from the overgrowth of opportunistic pathobionts already present in the microbiota[28,29]. Therefore, we assessed the potential differential impact of pretreatment with free Abx vs different Abx-loaded nanoparticles on the severity of a *C. rodentium* intestinal infection, a model frequently used to study enteropathogenic *E. Coli* infections in humans. Antibiotic pretreatment simulates the initial treatment and associated dysbiosis, followed up at day 5 by intestinal challenge

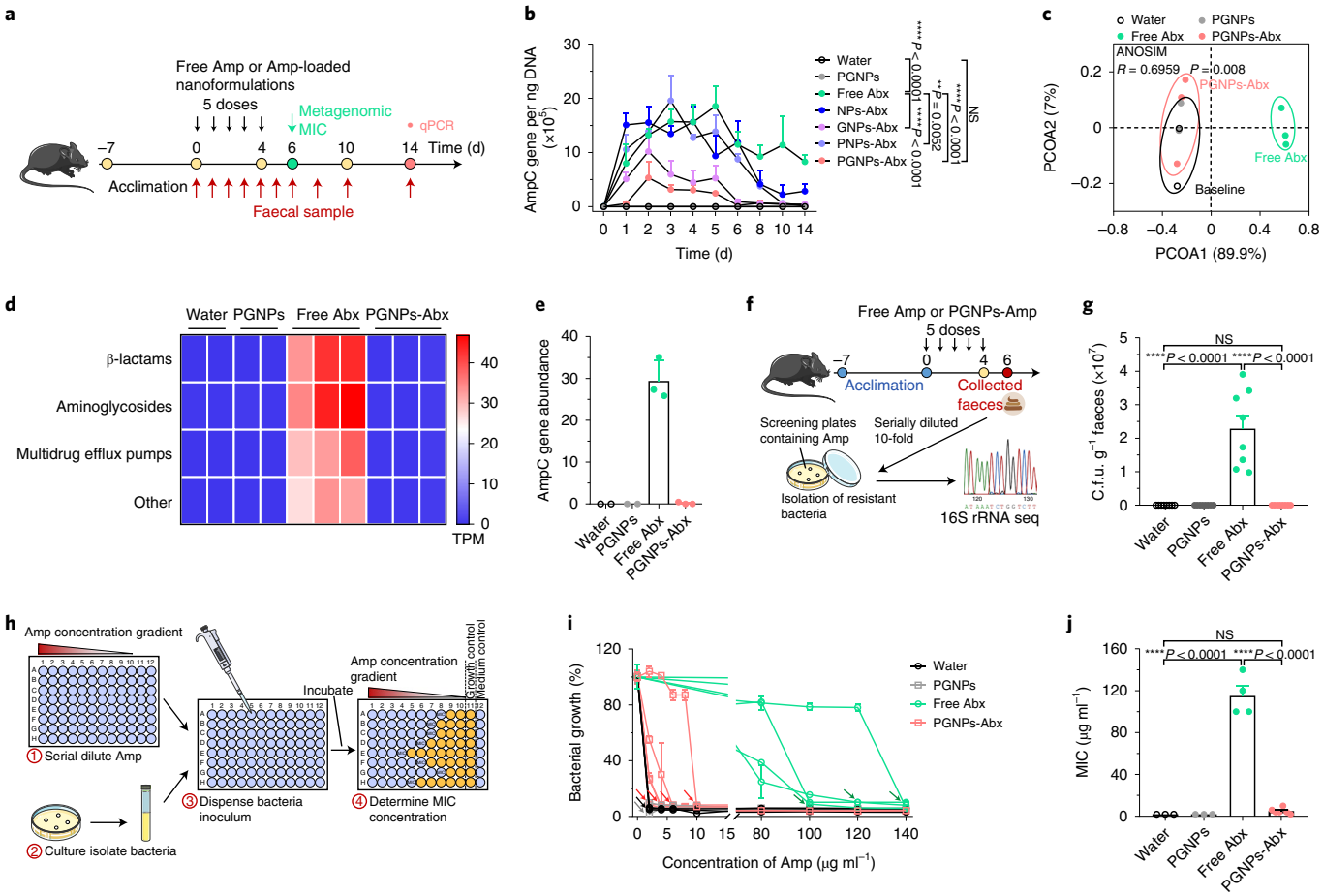

Fig. 8 | The PGNP-mediated delivery of antibiotics reduces antibiotic-resistance genes in gut microbiota. a, Schematic showing the experimental design. Mice received free Amp or Amp-loaded nanoparticles at 20 mg kg^{-1} body weight for 5 d consecutively, control mice (water and PGNPs group) lacked antibiotic treatment. Faecal samples were collected at the indicated time points, and total DNA was extracted for metagenomic sequencing or qPCR measurement of the known antibiotic-resistance gene (ARG). **b**, qPCR analysis to determine β-lactamase ampC gene copy number in faecal samples of indicated groups. $n \geq 4$ mice. **c**–**e**, Metagenomic sequencing analysis in the faecal samples of mice from indicated groups. Bray–Curtis-based beta diversity of control and antibiotics treatment groups based on ARG subtypes (**c**), abundance of detected ARGs. TPM, transcripts per kilobase of exon model per million mapped reads. (**d**) and β-lactamase ampC gene abundance (**e**), $n \geq 2$ mice. **f**, Schematic of the experimental design. Isolation of antibiotic-resistant bacteria in free Amp or PGNPs-Amp-treated mice using GAM plates with 20 μg ml^{-1} ampicillin. **g**, Quantification of the bacterial c.f.u.s under anaerobic condition. $n = 8$ mice. **h**, Drug susceptibility tests for antibiotic-resistant *Enterobacter* isolated from free Amp or PGNPs-Amp-treated mice under anaerobic conditions using GAM. **i**, Growth curve showing that the Amp susceptibility of *Enterobacter* isolated from free Amp was 100–140 μg ml^{-1} and that of *Enterobacter* isolated from PGNPs-Amp was 2–10 μg ml^{-1} under anaerobic condition. The arrows represent the MIC of each bacterial clone. **j**, Quantification MIC for data in **i**. $n \geq 3$ colonies. All values are expressed as mean ± s.e.m. Statistical significance was determined using two-way ANOVA in **a**, or one-way ANOVA with Tukey's multiple comparisons in **g** and **j**. $^*P < 0.05$, $^{**}P < 0.01$, $^{***}P < 0.001$, $^{****}P < 0.0001$. Data in **b**–**e** are representative of 3 independent experiments; **g**, **i** and **j** were repeated twice.

with the pathogenic *C. rodentium* (Fig. 7a). Mice pretreated for 5 d with free ampicillin and vancomycin displayed increased susceptibility to *C. rodentium* infection compared with control mice lacking pretreatment with antibiotics, which was evident from higher bacterial loads in faeces, caecum and colon, a heavier caecum and more extensive regions of mucosal hyperplasia (Fig. 7b–f and Extended Data Fig. 10). In contrast, there was no difference in the severity of the *C. rodentium* infections between PGNPs-Abx-pretreated and non-pretreated control mice (Fig. 7b–f and Extended Data Fig. 10), suggesting that PGNPs delivery protects the mice from dysbiosis-associated pathogen infections.

To test whether the protection of PGNPs against antibiotics-induced increased susceptibility to *C. rodentium* infections relies on SGLT1, we used phlorizin, the SGLT1 inhibitor (iSGLT1), to study the influence of PGNPs-Abx on *C. rodentium* infection with and without phlorizin. After pretreating the mice with phlorizin, we detected a notable increase in susceptibility to *C. rodentium* infection of PGNPs-Abx co-administered with the inhibitor compared with PGNPs-Abx alone, as evidenced by higher bacterial loads (in faeces, caecum and colon), a heavier caecum and more extensive regions of mucosal hyperplasia (Fig. 7b–f and Extended Data Fig. 10). No such difference was observed between PNPs-Abx alone and PNPs-Abx co-administered with iSGLT1 (Fig. 7b–f and Extended Data Fig. 10). These data indicate that PGNPs delivery protects mice from antibiotics-induced disturbance of microbiota, owing to the target absorption of nanoparticles by SGLT1 transporters in the proximal small intestine (Fig. 7g). These results support the idea that the delivery of antibiotics using glucosylated nanocarriers reduces susceptibility to pathogenic infections, avoiding dysbiosis of microbiota.

PGNPs delivery of antibiotics reduces antibiotic-resistance genes in gut microbiota. The rapid emergence of antibiotic-resistant bacteria continues to pose a major public health threat. Selective pressure from clinical applications, as well as growth-promotional use of antibiotics in food animal production, are major drivers of this health crisis[15,30]. Common life-threatening intestinal and systemic infections include antibiotics-resistant strains of pathogens including *Klebsiella pneumoniae*, *Staphylococcus aureus* and *Clostridium difficile*[1]. To assess potential differential effects of free vs antibiotics-loaded nanoparticles on the propensity of bacteria to develop antibiotic resistance, we used qPCR to assess differential copy number accumulation of a gene known to promote ampicillin resistance (lactamase ampC) in commensal bacteria present in faecal samples. The treatment of mice with free Amp led to strongly increased ampC copy numbers in faecal samples, whereas oral administration of PGNPs-Amp did not markedly alter the ampC copy number compared with the untreated control or other NPs groups (Fig. 8a,b).

We performed metagenomic sequencing of faecal samples from PGNPs-Amp/free-Amp-treated mice, where PCA analysis of antibiotic-resistance gene expression shows that PGNPs delivery globally prevents antibiotics-induced accumulation of antibiotic-resistance genes (Fig. 8c–e). We further isolated typical ampicillin-resistant strains using the Glfu anaerobic medium broth (GAM). Free Amp treatment resulted in more ampicillin-resistant colonies compared with the PGNPs-Amp treatment under anaerobic culture conditions. We validated this result by 16S rRNA sequencing, which showed that the majority of the colonies are made up of *Enterobacter* (Fig. 8f,g). We also performed the ampicillin susceptibility test to measure the minimal inhibitory concentration (MIC) to the resistant strains of *Enterobacter*, which showed that the strains isolated from free-Amp-treated mice can still grow at an 80 μg ml^{-1} concentration of Amp, while the isolated *Enterobacter* from PGNPs-Amp-treated mice and control mice did not grow at a 10 μg ml^{-1} concentration of Amp (Fig. 8h–j). These findings indicate that the PGNPs delivery strategy reduces the exposure of gut microbiota to antibiotics and attenuates induction of known antibiotic-resistance genes.

Discussion

Although antibiotics are nearly universally deployed as life-saving tools for the treatment of bacterial infections, their excessive use poses numerous risks to human health. This prompted us to develop an antibiotic-delivery technology that minimizes the impact of antibiotics on the gut microbiota. A previous study suggested the potential application of gold nanoparticles for treating bacterial infections without perturbation of microbiota[31]; however, other studies on gold and silver nanoparticles have reported that these materials actually do cause gut dysbiosis[32].

We have shown how a glucose-decorated antibiotic-delivery system enables the targeted and highly efficient uptake of antibiotics at the proximal small intestine—a region of the gut positioned in front of the largest (post-caecum) communities of microbiota—by mixing antibiotic molecules with the glucosylated nanocarriers. The PGNP system reduces perturbations to the microbiota and the oral delivery of PGNPs-Abx reduces dysbiosis-induced adverse effects.

Although preliminary and relying on murine models, our work suggests that PGNP-based antibiotic delivery can substantially reduce the severity of antibiotic-induced dysbiosis of gut microbiota. Such dysbiosis has many well-established clinical manifestations that can severely endanger patients and promote antibiotic-resistant pathogenic strains in hospitals. PGNPs-Abx enables convenient oral delivery of antibiotics and could potentially obviate the need for extensive hospitalizations, thus reducing associated costs and risks. We have shown that glucosylated nanocarriers perform efficiently for the delivery of ampicillin, chloramphenicol and vancomycin. In the future, it will be interesting to test whether this system performs well with other antibiotics and even other drugs with uptake-related or gut-dysbiosis-related limitations. The strong and selective uptake efficiency enabled by PGNPs suggests their potential use for the oral delivery of other drugs.

Methods

Animals. All experiments used 3–10-week-old, age- and sex-matched C57BL/6 mice. Mice were kept at a strict 12 h light–dark cycle, with lights on from 8:00 to 20:00. All animal experiments were approved by the Ethics Committee of the University of Science and Technology of China.

Materials. Chlorotrimethylsilane, hexamethyldisilazane, phlorizin and phloretin were purchased from Aladdin Reagent. Ampicillin, chloramphenicol and vancomycin were purchased from Sangon Biotech. Glycolide (GA) and D,L-lactide (LA) were purchased from Dai Gang Biomaterial. D-glucose was purchased from Sinopharm Chemical Reagent. Stannous octoate ($Sn(Oct)_2$) was purchased from Sigma-Aldrich. Lipid 1,2-dioleoyl-3-trimethylammonium-propane chloride (DOTAP) was purchased from Avanti Polar Lipids. 1,1′-Dioctadecyl-3,3,3′,3′-tetramethylindodicarbocyanine, 4—chlorobenzenesulfonate salt (DiD) and 3,3′-dioctadecyloxacarbocyanine perchlorate (DiO) were purchased from Biotium, and Rhodamine B (RhoB)-conjugated PLGA polymers (PLGA-RhoB) were synthesized according to previous literature[33]. Other chemicals and reagents were of analytical grade unless otherwise stated.

PEG-*b*-PLGA synthesis and preparation of NPs and PNPs. Poly(ethylene glycol)-*block*-poly(lactic-co-glycolic acid) (PEG-*b*-PLGA) was synthesized by ring-opening polymerization according to a previous report[34]. Briefly, a PEG (Mw 5,000, 5.0 g, Sigma-Aldrich) and a 3:1 molar ratio of LA (9.53 g)/GA (2.56 g) were added into a flask. Then, the catalyst $Sn(Oct)_2$ was added with PEG (1:1 molar ratio) and the reaction was allowed to proceed at 130 °C. After 2 h, the product was further dissolved in $CHCl_3$ and precipitated three times. The product was then dried under vacuum. The prepared block copolymers PEG-*b*-PLGA consisting of PEG (Mw, PEG = 5,000) and PLGA (Mw PLGA = 11,000, LA/GA = 75/25 (mol/mol)) were obtained according to ^{1}H NMR analysis. Nanoparticles were prepared by a double emulsion-solvent evaporation method. Briefly, 0.5 ml of dichloromethane containing 30 μl of Milli-Q water and 5 mg PEG-*b*-PLGA was emulsified by sonication (Vibra-cell, Sonics & Materials) at 80 W for 1 min in an ice bath. This primary oil-in-water emulsion was further emulsified in 5 ml of Milli-Q water by sonication (80 W for 1 min) in an ice bath to form a water-in-oil-in-water emulsion. Subsequently, the dichloromethane was removed by a rotary evaporator. Then, the resulting NPs were concentrated by ultrafiltration (molecular weight cut-off, 100,000 Da, Millipore) and stored at 4 °C for further use. For the preparation of positive nanoparticles (PNPs), the same procedure as for NPs was employed, except that 0.5 mg DOTAP was added to the dichloromethane solution before being emulsified by sonication.

Gluc-PEG-*b*-PLGA synthesis and preparation of GNPs and PGNPs. Detailed procedures for the synthesis of polymer Gluc-PEG-*b*-PLGA are provided in Supplementary Figs. 2 and 3. Glucosylated nanoparticles (GNPs) were similarly prepared as NPs using the same protocol, except that 5 mg PEG-*b*-PLGA was replaced with 5 mg Gluc-PEG-*b*-PLGA. Positive glycosylated nanoparticles (PGNPs) were similarly prepared as NPs using the same protocol, except that 5 mg PEG-*b*-PLGA was replaced with 5 mg Gluc-PEG-*b*-PLGA, and 0.5 mg DOTAP was added to the dichloromethane solution before being emulsified by sonication. A series of PGNPs with varying densities of glucose ligands on their surface were prepared by changing the blending ratio between Gluc-PEG-*b*-PLGA and PEG-*b*-PLGA (molar ratio, 0:100, 33:67, 67:33, 100:0). PGNPs of different sizes were prepared by changing the molar ratios of Gluc-PEG-*b*-PLGA and homopolymer PLGA (Mw 7,000, LA/GA = 75/25 (mol/mol)).

Characterization of NPs, PNPs, GNPs and PGNPs. The size and zeta potential of NPs, PNPs, GNPs and PGNPs were determined by dynamic light scattering (DLS). The temperature was set to 25 °C and the detection was repeated three times, each repeat comprising 20 cycles with a 10 s pause after each cycle. The morphologies of NPs were examined by TEM (JEOL2010). The prepared NPs were dissolved in Milli-Q water to 0.3 mg ml^{-1}, and then repeatedly dripped onto the surface of a 230-mesh thin copper grid and immediately air-dried. At a constant temperature of 25 °C, the morphology of nanoparticles was detected by the TEM at an acceleration voltage of 200 kV.

Preparation of DiD or RhoB-labelled NPs, PNPs, GNPs and PGNPs. To 0.5 ml of the aforementioned nanoparticles (NPs, PNPs, GNPs or PGNPs) in dichloromethane solution, 12.5 μg fluorescent dye DiD or 0.5 mg PLGA-RhoB was added. Then the solutions were emulsified by sonication.

Biodistribution of nanoparticles. C57BL/6 mice (6–8 weeks old) were fasted for 6 h and orally administered NPs-DiD, PNPs-DiD, GNPs-DiD or PGNPs-DiD at

0.42 mg kg^{-1} body weight. The mice were killed at 1 h after injection and excess blood was washed out by perfusion with PBS. The liver, kidney, spleen, heart and lung were excised, rinsed with PBS, weighed after removing excess fluid and homogenized with cell lysis buffer. The accumulated NPs were quantified by measurement of fluorescence signal intensity using a Hitachi F-4600 fluorescence spectrophotometer.

In vivo uptake dynamics of DiD-labelled nanoparticles in intestine. C57BL/6 mice (6–8 weeks old) were fasted for 6 h before the experiment. Free DiD, NPs-DiD, PNPs-DiD, GNPs-DiD and PGNPs-DiD were orally administered to mice at 0.42 mg kg^{-1} body weight. Faecal samples were collected at 0–1, 1–4, 4–8 and 8–12 h periods, and placed into 24-well plates to measure fluorescence signals. At the indicated time points, mice were killed, and the digestive tract was isolated and rinsed with PBS. The distribution of DiD fluorescence in the intestines was determined using the IVIS spectrum (Perkin Elmer). Caecal contents were collected at 12 h post oral gavage and immediately analysed using IVIS.

Inhibition of glucose transporters in vivo. To examine the effect of SGLT1 and GLUT2 inhibitor on the intestine accumulation of PNPs and PGNPs, C57BL/6 mice were intragastrically administered with 50 mg kg^{-1} phlorizin (Aladdin), 30 mg kg^{-1} mizagliflozin (MedChemExpress, MCE), or 50 mg kg^{-1} mg phloretin (Aladdin) 1 h before oral administration of PNPs-DiD or PGNPs-DiD. The intestinal uptake of nanoparticles was determined using IVIS, as described above.

Pharmacokinetics of DiD-labelled nanoparticles in vivo. C57BL/6 mice (6–8 weeks old) were treated with Free DiD, NPs-DiD, PNPs-DiD, GNPs-DiD or PGNPs-DiD by oral gavage. The hairs on the skin of the ear were carefully removed using depilatory cream. After 30 min, mice were anaesthetized and intravenously administered with DiO-labelled PEG-*b*-PLGA polymeric micelles (NPs-DiO) for visualization of the ear vasculature. NPs-DiO immediately revealed the vascular structure upon blood vessel perfusion. The ear was then real-time visualized using CLSM (Nikon). Images were taken every 2 min for up to 4 h. The excitation wavelength for nanoparticles was 633 nm. Images were processed with Image J software.

Plasmids. Mouse SGLT1 (NCBI accession number NM_019810.4, NP_062784.3) and GLUT2 (NCBI accession number NM_031197.2, NP_112474.2) were reverse transcribed, PCR amplified and cloned into GFP-N1 vector (Addgene number 122162).

Cellular uptake of PNPs-DiD and PGNPs-DiD. HEK293T cells (ATCC CRL-3216) were cultured in DMEM medium supplied with 10% FBS, 1% penicillin and streptomycin. Cells were seeded overnight in a 6 cm dish and then transfected with 2 μg SGLT1-GFP and GLUT2-GFP plasmid by Lipofectamine 2000 (Thermo Fisher). After 24 h post transfection, cells were plated on glass plates (Nest) and incubated for 6 h at 37 °C in a 5% CO_2 incubator. Subsequently, 100 μl PGNPs-DiD or PNPs-DiD were added and further incubated for 1 h. Living cells were observed by CLSM to evaluate the cellular uptake of nanoparticles.

Preparation of antibiotics-loaded nanoparticles. The preparation of antibiotics-loaded nanoparticles was similarly achieved as with NPs, PNPs, GNPs and PGNPs using the same protocol, except that ampicillin, vancomycin (30 μl, 100 mg ml^{-1} in Milli-Q water) or chloramphenicol (50 μl, 50 mg ml^{-1} in ethyl acetate) was added to 0.5 ml dichloromethane solution before being emulsified by sonication. The obtained antibiotics-loaded nanoparticles were washed three times using an ultrafiltration tube with Milli-Q water to remove free antibiotics.

Measurement of antibiotics concentration. C57BL/6 mice (6–8 weeks old) were randomly divided into five groups. All experimental animals intragastrically received a single-dose antibiotic (40 mg kg^{-1} of ampicillin or 8 mg kg^{-1} of chloramphenicol) or antibiotic-loaded nanoparticles. Blood samples (200 μl) were collected into tubes at 1, 2 and 4 h post administration. The blood samples were centrifuged for 15 min (4 °C, 4,000 r.p.m.) to separate serum for further analyses. Mice were killed at 4 h, and the intestine, heart, liver, spleen and lung were collected, weighed and homogenized in water. The homogenized organs were centrifuged for 10 min (4 °C, 10,000 r.p.m.) and the supernatant was transferred into new tubes. Acetonitrile was added to the collected supernatant at a 9:1 volume, vortexed for 1 min, mixed well and centrifuged for 10 min (4 °C, 10,000 r.p.m.). The standard substance ampicillin or chloramphenicol was added into blank serum to prepare standard substance solutions with concentrations of 1, 2, 5, 10, 20, 50 and 100 ng ml^{-1}. The solution was filtered through a 0.22 μm membrane, and concentrations of antibiotics in blood and organs were subsequently analysed by liquid chromatography-tandem mass spectrometry (LC–MS/MS) as previously described[35–37].

Lung infection model with *S. pneumoniae*. Pneumonia was induced by intranasal inoculation with 3×10^8 c.f.u.s *S. pneumoniae* in 40 μl PBS as previously described[38]. Free ampicillin (40 or 200 mg kg^{-1}) or the same dose of PGNPs-encapsulated ampicillin (40 mg kg^{-1}) was orally administered to mice at 2 and 10 h post infection, respectively. Lung samples were collected and analysed at 24 h after induction of pneumonia. For c.f.u. counts, lungs were collected and homogenized in three volumes of PBS. For bacterial quantification, lung homogenates were serially diluted 10-fold in PBS and plated onto sheep-blood agar plates. After overnight incubation at 37 °C, c.f.u.s were counted. For cytokine mRNA measurement, RNA was isolated from the precipitation of lung homogenates and real-time PCR was used to measure cytokine expression.

Bacteremia model with *L. monocytogenes*. Sepsis was induced by retro-orbital injections with 2×10^6 c.f.u.s *L. monocytogenes* in 100 μl PBS. Free ampicillin (40 mg kg^{-1}) or the same dose of PGNPs-encapsulated ampicillin was orally administered to mice at 2 and 8 h post infection. For the determination of bacterial counts in sepsis, peripheral blood samples were collected at 24 h post infection. The 100 μl blood volume was brought up to 1 ml with distilled water and 10-fold serially diluted in water and plated onto tryptone soya broth (TSB) plates. At the same time point, the liver and spleen were also collected, weighed and homogenized in a 1 ml volume of water, then 10-fold serially diluted in water, plated onto TSB plates and incubated at 37 °C overnight. Colonies were counted for c.f.u.s calculation.

16S rRNA-microbiota sequencing. Faecal samples were taken from mice at the indicated time points and stored at −80 °C until 16S rRNA analysis. DNA was extracted from faecal pellets with a QIAamp stool DNA mini kit, following the vendor's instructions (QIAGEN). 16S rRNA amplicons were generated using the primer 515F/806R recommended by the Earth Microbiome Project2. The primer sequences included the 515F forward barcode primer: AATGATACGGCGACCACCGAGATCTACACGCTXX XXXXXXXXXXTATGGTAATTG TGTGYCAGCMGCCGCGGTAA and 806R reverse primer: CAAGCAGAAGACGGCATACGAGATAGTCAGCC AGCCGGACTACNVGGGTWTCTAAT. PCR products were quantified, pooled and cleaned using the PCR Cleanup kit (QIAGEN) and subsequently sequenced using 250 bp paired-end sequencing (Illumina MiSeq V3 kit) to an average depth of 29,292 ± 11,228 reads (mean ± s.d.). The sequences were then further processed using a customized pipeline that combined usearch 3 (v8.1), vsearch 4 (v2.13.0) and QIIME 2 (v1.9.1). Taxonomic classification was performed using the Ribosommal Database Project-classifier and an Operational Taxonomic Units (OTU) table was created. For beta diversity, unweighted UniFrac measurements were plotted according to the first two principal coordinates on the basis of 5,000 reads per sample. ANOSIM analyses were performed with the vegan package (v2.5-7) in R (v4.0.5) to compare the similarities among different groups.

HFD mouse model. C57BL/6J mice (3 weeks old, male) were fed with free antibiotics or antibiotics-loaded nanoparticles via intragastric gavage daily for 5 d, as described above. All mice were switched to HFD (Rodent Diet MD12033, Research Diets, 60% kcal from fat) from 7 to 19 weeks of age. The body weight was monitored weekly throughout HFD feeding. The intraperitoneal glucose tolerance test (IPGTT) was performed after 10 weeks of HFD feeding. Briefly, mice were intraperitoneally injected with glucose dissolved in sterile water at 1 g kg^{-1} body weight following 16 h of fasting. Before (time 0) and after (15, 30, 60 and 120 min) the IP glucose injection, blood glucose levels were measured with a glucometer (Sinocare). Mice were then killed for further analysis after 12 weeks of HFD feeding. Total, visceral and subcutaneous fat were dissected from male mice and weighed. Livers were excised, weighed and homogenized with a 4-fold volume of PBS. After centrifugation at 12,000 r.p.m. for 10 min, the supernatant was collected for the following analysis. Serum was collected via the retro-orbital plexus and centrifuged at 4,000 r.p.m. for 15 min. Subsequently, total cholesterol levels of liver suspension and serum were assessed using a total cholesterol assay kit (Nanjing Jiancheng Bioengineering Institute) following the manufacturer's instructions.

Faecal microbiota transplantation. Faecal microbiota transplantation (FMT) was performed according to a reported protocol[39]. Briefly, donor mice were given water, PGNPs, free antibiotics or antibiotics-loaded PGNPs daily for 5 d. Faecal pellets were collected for FMT in sterile conditions. The pellets from each donor mouse were separately resuspended in sterile PBS under anaerobic conditions with vigorous mixing and allowed to settle by gravity for 2 min. Samples were immediately transferred to the animal facility and the supernatant was administered to recipient mice whose commensal microbes were depleted using antibiotics including ampicillin (1 g l^{-1}), vancomycin (0.5 g l^{-1}), neomycin sulfate (1 g l^{-1}) and metronidazole (1 g l^{-1}) in their drinking water for two weeks. Then, the recipient mice were fed with HFD for 13 weeks and analysed as described above.

Intestinal infection model with *C. rodentium*. Mice (6–8 weeks old) were pretreated with free antibiotics (20 mg kg^{-1} ampicillin and 20 mg kg^{-1} vancomycin) or the same dose of antibiotics-loaded nanoparticles for 5 d via gavage feeding. Control mice received the same volume of 200 μl water or PGNPs by oral administration. Then, all groups of mice were challenged with *C. rodentium* via intragastric gavage. Briefly, *C. rodentium* (strain DBS100) was prepared by shaking the bacteria in Luria-Bertani broth at 37 °C overnight. Mice were infected with 5×10^8 c.f.u.s *C. rodentium* in a total volume of 200 μl per mouse by oral gavage and analysed on day 8 post infection. The distal colon, caecum and faecal specimen

were removed aseptically, weighed and homogenized in PBS. Then, the tissue homogenates were serially diluted in PBS, plated on MacConkey agar plates and incubated overnight at 37 °C. Bacterial colonies were enumerated and normalized to the tissue weight (c.f.u.s per gram). To test the role of SGLT1 transporter, mice were first orally gavaged with phlorizin at 50 mg kg^{-1} body weight 1 h before oral administration with PNPs-Abx or PGNPs-Abx, then challenged with *C. rodentium* as described above.

Metagenomic sequencing and analysis. Total DNA was extracted (QIAamp stool DNA mini kit, QIAGEN) for metagenomic sequencing. For original paired-end data, fastQC (V0.11.5) was used for initial quality control and Trimmomatic (V0.39) was used for trimming. The parameters are the following: LEADING, 20; TRAILING, 20; MINLEN, 90. Megahit (V1.2.9) was used to join the clipped data to retain contigs within >1 KB, then CD-hit (v4.8.1) was used to merge contigs with 99% identity, and Minimus2 was used to merge again (parameter: minimum overlap, 100 bp; at least 95% identity). The combined contig used Prodigal (V2.6.3) for gene prediction. The resistance genes were compared with CARD database by Abricate (V1.0.1) (parameters: query coverage >90% and sequence identity >70%). Salmon (v1.5.1), a non-mapping-based method, was used to obtain gene counts and directly determine their relative abundance.

MIC test. Strains for the MIC assay were selected on non-selective solid medium before experiments. A total of 2–6 well-isolated colonies of the same morphological type were selected and transferred into tubes, each containing 5 ml of broth medium. The broth was incubated in an anaerobic incubator at 37 °C until its optical density $(OD)_{600}$ reached approximately 0.4. The suspension was diluted to 1:200 to obtain a tube containing about 1×10^6 c.f.u.s ml^{-1}. The following step was used to prepare the suitable dilution series of antibiotics (the antibiotic dilutions were prepared at double the desired concentration). The antibiotic dilutions (75 µl) were serially added to a sterile 96-well plate, and the same volumes of bacterial suspensions were added, resulting in a suspension containing approximately 5×10^5 c.f.u.s ml^{-1} and a 1:2 dilution of each antibiotic concentration. After incubating the 96-well plate at 37 °C for 24–48 h in an anaerobic incubator, the MIC was read as the lowest concentration of antibiotics that completely inhibited bacterial growth in the wells. Each group of a certain concentration in the dilution series was performed with three parallel samples.

Real-time PCR. Total RNA was extracted from lung cells and human intestinal tissues using the trizol reagent (TIANGEN). Complementary DNA was synthesized with a reverse transcriptase kit according to the manufacturer's protocol (Vazyme). Real-time PCR was performed using SYBR Green master mix (Vazyme) on the CFX384 Real-Time System (Bio-Rad). The relative expression of target genes was first normalized to the internal control (Hprt/Gapdh), then the fold-changes between groups were calculated using 2^(−ΔCt). The copy number per nanogram of DNA for each sample was then calculated using the slope of the standard curve as previously described[40,41]. The primers used are listed below.

SGLT1 forward: GTCATCTCCCTCCTCACCAA. SGLT1 reverse: TCCAG GTCAAT ACGCTCCTC. SGLT2 forward: TACTTCGCCATTGTGCTGTT. SGLT2 reverse: CTCCCGTTCCTCCTTGCT. Gapdh forward: GGTGGT CTCCTCTGACTTCAACA. Gapdh reverse: GTTGCTGTAGCCAAATTCGTTGT. IL-1β forward: CTACAGGCTC CGAGATGAACAAC. IL-1β reverse: TCCATT GAGGTGGAGAGCTTTC. IL-6 forward: GATGGATGCTACCAAACTGGAT. IL-6 reverse: CCAGGTAGCTATGGT ACTCCAGA. TNF-α forward: GACGT GGAACTGGCAGAAGAG. TNF-α reverse: TTGGTGGTTTGTGAGTGTGAG. Hprt forward: ACCTCTCGAAGTGTTGGATACAGG. Hprt reverse: CTTGC GCTCATCTTAGGCTTTG. S24-7 forward: CGGATTTATTG GGTTTAAAGG GT. S24-7 reverse: ATCTATGCATTTCACCGCTACACCA. Rikenellaceae forward: ATTGGGT TTAAAGGGTGCGTAG. Rikenellaceae reverse: TGCCTT CGCAATCGGTGTTCT. AmpC forward: TGAGTTAGGTTCGGTCAGCA. AmpC reverse: AGTATTTTGTTG CGGGATCG.

Hematoxylin and eosin staining. Tissues were fixed in 4% paraformaldehyde (PFA) and embedded in paraffin. Sections were stained with haematoxylin and eosin. Morphological changes in the stained sections were examined under a light microscope (TissueFAXS PLUS). Lung and liver sections were scored according to both histological and morphometric analysis as previously described[42–44].

Immunofluorescence staining. The small intestine and colon tissue were isolated, fixed in 4% PFA overnight, washed with PBS, cryo-protected in 30% sucrose solution overnight, then processed through optimal cutting temperature compound embedding, and finally cut into 10-µm-thin sections. The primary antibodies for immunofluorescence were rabbit Rab11a antibody (2413, Cell Signaling Technology) and rabbit SGLT1 antibody (20801, BiCell Scientific). These antibodies were incubated in 1% diluted blocking buffer overnight at dilutions of 1:100 at 4 °C; the sections were washed with PBS and incubated with a secondary antibody (A-11071) at dilutions of 1:200 in 1% blocking buffer for 1 h at room temperature. Subsequently, sections were washed with PBS, counterstained with DAPI (1 µg ml^{-1}) in PBS for 10 min and examined using CLSM.

For Rab11a staining in HEK293T cells, briefly, cells were plated on glass plates (Nest) and incubated for 6 h at 37 °C in a 5% CO_2 incubator. Subsequently, 100 µl PGNPs-DiD were added, followed by further incubation for 2 h. Then, cells were fixed in 4% PFA for 30 min and blocked with 1% BSA in PBS for 30 min. The fixed cells were incubated overnight with Rab11a antibody in 1% diluted blocking buffer at 4 °C. The slides were then washed three times with PBS and incubated with a secondary antibody for 1 h at 37 °C. The co-localization of Rab11a with PGNPs in images was calculated using Image J software.

Flow cytometry. Single-cell suspensions were stained with FACS antibodies in FACS buffer (PBS with 2% BSA and 5 mM EDTA) for 20 min at 4 °C. The antibodies used were APC/Cy7 anti-CD45.2 (Biolegend, clone 104), PE/Cy7 anti-CD11b (Biolegend, clone M1/70), FITC anti-Ly6G (Biolegend, clone 1A8), and PE anti-CD14 (Biolegend, clone Sa14-2). Flow cytometric analyses were performed on a cytometer (FACSVerse, BD Biosciences) and analysed using FlowJo v.10.0.7 software.

Biosafety analysis. Healthy C57BL/6 mice were orally administered with PGNPs or water for 5 d, then weighed every day for 10 additional days. Mice were killed, and the livers, kidneys, spleens, hearts and lungs were collected and fixed in 4% PFA for haematoxylin and eosin staining. Histological morphology was examined using a light microscope (TissueFAXS PLUS). Blood cell numbers were counted, and serum alanine aminotransferase and uric acid concentrations were measured using a commensal kit (CHANGCHUN HUILI BIOTECH).

Bile acids measurements. Bile acid detection was performed by Applied Protein Technology. The faecal samples (30 mg) were homogenized in 200 µl of prechilled ultrapure water using an MP homogenizer. Then, 500 µl of prechilled methanol was added and mixed thoroughly by vortexing. The mixture was centrifuged at 14,000 *g* for 15 min at 4 °C, and then 100 µl of the supernatant was collected and mixed with 500 µl of 50% methanol and 10 µl of internal standard by vortexing, followed by incubation for 20 min at −20 °C to precipitate proteins. The supernatant was collected for analysis after 15 min centrifugation (14,000 *g*, 4 °C). Ultra performance liquid chromatography (UPLC) separation was achieved using a Waters ACQUITY UPLC I-Class system. The mobile phase consisted of solvent A (0.1% aqueous formic acid) and solvent B (methanol). A total of 2 µl sample aliquot was injected into the column via an auto sampler. The column and auto sampler temperatures were 40 and 6 °C, respectively, and the flow rate was 300 µl min^{-1}.

The chromatographic gradient set for mobile phase B was as follows: 0–6 min: from 60% to 65% B; 6–13 min: from 65% to 80% B; 13–13.5 min: from 80% to 90% B; 13.5–15 min: 90% B. Quality Control sample was used for testing and evaluating the stability and repeatability of the system. Finally, quantitation was achieved by MS detection in a negative ion mode using a 5500 QTRAP mass spectrometer (AB SCIEX). The 5500 QTRAP ESI source conditions were: source temperature, 550 °C; ion source gas1, 55; ion source gas2, 55; curtain gas, 40; ion spray voltage floating, −4,500 V; operated in the MRM model for ion-pair assay. The chromatographic peak area and retention time were calculated by Multiquant software. The standard curve was generated and used to calculate the content of bile acids in the samples.

Serum endotoxin detection. Lipopolysaccharide (LPS) concentrations in serum were determined by an endotoxin assay on the basis of a chromogenic limulus amoebocyte lysate (LAL) assay (ToxinSensor Chromogenic LAL endotoxin assay kit). All equipment and materials used for serum sample testing were endotoxin-free and provided by the endotoxin assay kit. The endotoxin content was expressed as endotoxin units per millilitre (EU ml^{-1}), and a measurable endotoxin concentration ranging from 0.01 to 10 EU ml^{-1} could be achieved.

Statistical analysis. The sample size for our animal experiments in this study was estimated on the basis of our previous experience of performing similar sets of experiments. All animal results were included and no randomization method was applied. For all bar graphs, data are expressed as mean ± s.e.m. or s.d. Statistical analysis was performed using unpaired Student's *t*-tests for two groups and one-way analysis of variance (ANOVA) or two-way ANOVA (GraphPad Prism software) for multiple groups, with all data points showing a normal distribution. To compare two non-parametric data sets, a Mann–Whitney *U*-test was employed. P values < 0.05 were considered significant. The sample sizes (biological replicates), specific statistical tests and the main results of our statistical analyses for each experiment are detailed in each figure legend.

Reporting summary. Further information on research design is available in the Nature Research Reporting Summary linked to this article.

Data availability

The main data supporting the results in this study are available within the paper and its Supplementary Information. All sequence data generated in this study are available from the SRA database with accession numbers PRJNA666621 and PRJNA666612. Source data are provided with this paper.

Received: 10 February 2021; Accepted: 20 May 2022;
Published online: 7 July 2022

References

1. Lynch, S. V. & Pedersen, O. The human intestinal microbiome in health and disease. *N. Engl. J. Med.* **375**, 2369–2379 (2016).
2. Levison, M. E. Pharmacokinetics and pharmacodynamics of antibacterial agents. *Infect. Dis. Clin. North Am.* **23**, 791–815 (2009).
3. Leffler, D. A. & Lamont, J. T. *Clostridium difficile* infection. *N. Engl. J. Med.* **372**, 1539–1548 (2015).
4. Brown, K. A., Khanafer, N., Daneman, N. & Fisman, D. N. Meta-analysis of antibiotics and the risk of community-associated *Clostridium difficile* infection. *Antimicrob. Agents Chemother.* **57**, 2326–2332 (2013).
5. Baumler, A. J. & Sperandio, V. Interactions between the microbiota and pathogenic bacteria in the gut. *Nature* **535**, 85–93 (2016).
6. Kim, Y. G. et al. Gut dysbiosis promotes M2 macrophage polarization and allergic airway inflammation via fungi-induced PGE_2. *Cell Host Microbe* **15**, 95–102 (2014).
7. Cho, I. et al. Antibiotics in early life alter the murine colonic microbiome and adiposity. *Nature* **488**, 621–626 (2012).
8. Cox, L. M. et al. Altering the intestinal microbiota during a critical developmental window has lasting metabolic consequences. *Cell* **158**, 705–721 (2014).
9. Sommer, M. O. A., Dantas, G. & Church, G. M. Functional characterization of the antibiotic resistance reservoir in the human microflora. *Science* **325**, 1128–1131 (2009).
10. Salyers, A. A., Gupta, A. & Wang, Y. P. Human intestinal bacteria as reservoirs for antibiotic resistance genes. *Trends Microbiol.* **12**, 412–416 (2004).
11. Stiefel, U. et al. Oral administration of beta-lactamase preserves colonization resistance of piperacillin-treated mice. *J. Infect. Dis.* **188**, 1605–1609 (2003).
12. Léonard, F., Andremont, A., Leclerq, B., Labia, R. & Tancrède, C. Use of beta-lactamase-producing anaerobes to prevent ceftriaxone from degrading intestinal resistance to colonization. *J. Infect. Dis.* **160**, 274–280 (1989).
13. Khoder, M., Tsapis, N., Domergue-Dupont, V., Gueutin, C. & Fattal, E. Removal of residual colonic ciprofloxacin in the rat by activated charcoal entrapped within zinc-pectinate beads. *Eur. J. Pharm. Sci.* **41**, 281–288 (2010).
14. De Gunzburg, J. et al. Targeted adsorption of molecules in the colon with the novel adsorbent-based medicinal product, dav132: a proof of concept study in healthy subjects. *J. Clin. Pharmacol.* **55**, 10–16 (2015).
15. Zhang, L., Huang, Y., Zhou, Y., Buckley, T. & Wang, H. H. Antibiotic administration routes significantly influence the levels of antibiotic resistance in gut microbiota. *Antimicrob. Agents Chemother.* **57**, 3659–3666 (2013).
16. Mowat, A. M. & Agace, W. W. Regional specialization within the intestinal immune system. *Nat. Rev. Immunol.* **14**, 667–685 (2014).
17. Chen, L., Tuo, B. & Dong, H. Regulation of intestinal glucose absorption by ion channels and transporters. *Nutrients* **8**, 43 (2016).
18. Han, X. et al. Zwitterionic micelles efficiently deliver oral insulin without opening tight junctions. *Nat. Nanotechnol.* **15**, 605–614 (2020).
19. Cherazard, R. et al. Antimicrobial resistant *Streptococcus pneumoniae*: prevalence, mechanisms, and clinical implications. *Am. J. Ther.* **24**, 361–369 (2017).
20. Palleja, A. et al. Recovery of gut microbiota of healthy adults following antibiotic exposure. *Nat. Microbiol.* **3**, 1255–1265 (2018).
21. Suez, J. et al. Post-antibiotic gut mucosal microbiome reconstitution is impaired by probiotics and improved by autologous FMT. *Cell* **174**, 1406–1423 (2018).
22. Vangay, P., Ward, T., Gerber, J. S. & Knights, D. Antibiotics, pediatric dysbiosis, and disease. *Cell Host Microbe* **17**, 553–564 (2015).
23. Turnbaugh, P. J. et al. An obesity-associated gut microbiome with increased capacity for energy harvest. *Nature* **444**, 1027–1031 (2006).
24. Thomas, C., Pellicciari, R., Pruzanski, M., Auwerx, J. & Schoonjans, K. Targeting bile-acid signalling for metabolic diseases. *Nat. Rev. Drug. Discov.* **7**, 678–693 (2008).
25. Zhao, L. The gut microbiota and obesity: from correlation to causality. *Nat. Rev. Microbiol.* **11**, 639–647 (2013).
26. McGlone, E. R. & Bloom, S. R. Bile acids and the metabolic syndrome. *Ann. Clin. Biochem.* **56**, 326–337 (2019).
27. Wahlström, A. et al. Induction of farnesoid X receptor signaling in germ-free mice colonized with a human microbiota. *J. Lipid Res.* **58**, 412–419 (2017).
28. Wlodarska, M. et al. Antibiotic treatment alters the colonic mucus layer and predisposes the host to exacerbated *Citrobacter rodentium*-induced colitis. *Infect. Immun.* **79**, 1536–1545 (2011).
29. Buffie, C. G. et al. Profound alterations of intestinal microbiota following a single dose of clindamycin results in sustained susceptibility to *Clostridium difficile*-induced colitis. *Infect. Immun.* **80**, 62–73 (2012).
30. Peng, Z. et al. Update on antimicrobial resistance in *Clostridium difficile*: resistance mechanisms and antimicrobial susceptibility testing. *J. Clin. Microbiol.* **55**, 1998–2008 (2017).
31. Li, J. J. et al. Gold nanoparticles cure bacterial infection with benefit to intestinal microflora. *ACS Nano* **13**, 5002–5014 (2019).
32. Van den Brule, S. et al. Dietary silver nanoparticles can disturb the gut microbiota in mice. *Part. Fibre Toxicol.* **13**, 38–54 (2016).
33. Sun, C. Y. et al. Facile generation of tumor-pH-labile linkage-bridged block copolymers for chemotherapeutic delivery. *Angew. Chem. Int. Ed. Engl.* **55**, 1010–1014 (2016).
34. Zhao, J., Pahovnik, D., Gnanou, Y. & Hadjichristidis, N. Sequential polymerization of ethylene oxide, ε-caprolactone and l-lactide: a one-pot metal-free route to tri- and pentablock terpolymers. *Polym. Chem.* **5**, 3750–3753 (2014).
35. Ramos, M. et al. Determination of chloramphenicol residues in shrimps by liquid chromatography-mass spectrometry. *J. Chromatogr. B* **791**, 31–38 (2003).
36. Gonçalves, T. M. et al. Determination of ampicillin in human plasma by solid-phase extraction-liquid chromatography-tandem mass spectrometry (SPE-LC-MS/MS) and its use in bioequivalence studies. *Arzneim. Forsch.* **58**, 91–96 (2008).
37. Nalbant, D. et al. Development and validation of a simple and sensitive LC-MS/MS method for quantification of ampicillin and sulbactam in human plasma and its application to a clinical pharmacokinetic study. *J. Pharm. Biomed. Anal.* **196**, 113899 (2021).
38. Schuijt, T. J. et al. The gut microbiota plays a protective role in the host defence against pneumococcal pneumonia. *Gut* **65**, 575–583 (2016).
39. Pernigoni, N. et al. Commensal bacteria promote endocrine resistance in prostate cancer through androgen biosynthesis. *Science* **374**, 216–224 (2021).
40. Böckelmann, U. et al. Quantitative PCR monitoring of antibiotic resistance genes and bacterial pathogens in three European artificial groundwater recharge systems. *Appl. Environ. Microbiol.* **75**, 154–163 (2009).
41. Fernando, D. M. et al. Detection of antibiotic resistance genes in source and drinking water samples from a first nations community in Canada. *Appl. Environ. Microbiol.* **82**, 4767–4775 (2016).
42. Smith, K. M. et al. Prolonged partial liquid ventilation using conventional and high-frequency ventilatory techniques: gas exchange and lung pathology in an animal model of respiratory distress syndrome. *Crit. Care Med.* **25**, 1888–1897 (1997).
43. Kleiner, D. E. et al. Design and validation of a histological scoring system for nonalcoholic fatty liver disease. *Hepatology* **41**, 1313–1321 (2005).
44. Dieleman, L. A. et al. Chronic experimental colitis induced by dextran sulphate sodium (DSS) is characterized by Th1 and Th2 cytokines. *Clin. Exp. Immunol.* **114**, 385–391 (1998).

Acknowledgements

We thank Y. Yang for analysing the metagenomic sequencing results, J. Wang for helping with animal experiments, H. Tan for helping with microbial experiments, Q. Liang, H. Pan and C. Zeng for helping with the material experiments; Z. Tian, R. Zhou, W. Pan, R. Flavell, X. Song, K. Zhang, H. Ma and W. Wen for helpful discussion and comments on this patent-pending work. This work was supported by grants from the National Key R&D Program of China (2017YFA0205600 to Y.W. and 2018YFA0508000 to S.Z.), the Strategic Priority Research Program of the Chinese Academy of Sciences (XDB29030101 to S.Z.), the National Natural Science Foundation of China (52025036 to Y.W., 82061148013 and 81821001 to S.Z. and 51903105 to W.J.) and the Shanghai Municipal Science and Technology Major Project (S.Z.).

Author contributions

G.Z. and Q.W. designed, performed and interpreted experiments. W.T. designed and analysed the 16S rRNA and metagenomic sequencing results. W.J. designed and synthesized the polymers. W.J. helped with animal experiments and cellular experiments. E.E. provided analytical tools, critical comments and suggestions; S.Z., Y.W., G.Z. and Q.W. wrote the manuscript. E.E. edited the manuscript. Y.W. and S.Z. supervised the project.

Competing interests

E.E. is a consultant at Daytwo and BiomX in topics unrelated to the subject of this work. The other authors declare no competing interests.

Additional information

Extended data is available for this paper at https://doi.org/10.1038/s41551-022-00903-4.

Supplementary information The online version contains supplementary material available at https://doi.org/10.1038/s41551-022-00903-4.

Correspondence and requests for materials should be addressed to Yucai Wang or Shu Zhu.

Peer review information *Nature Biomedical Engineering* thanks Jian-Dong Jiang, Xian-Zheng Zhang and the other, anonymous, reviewer(s) for their contribution to the peer review of this work.

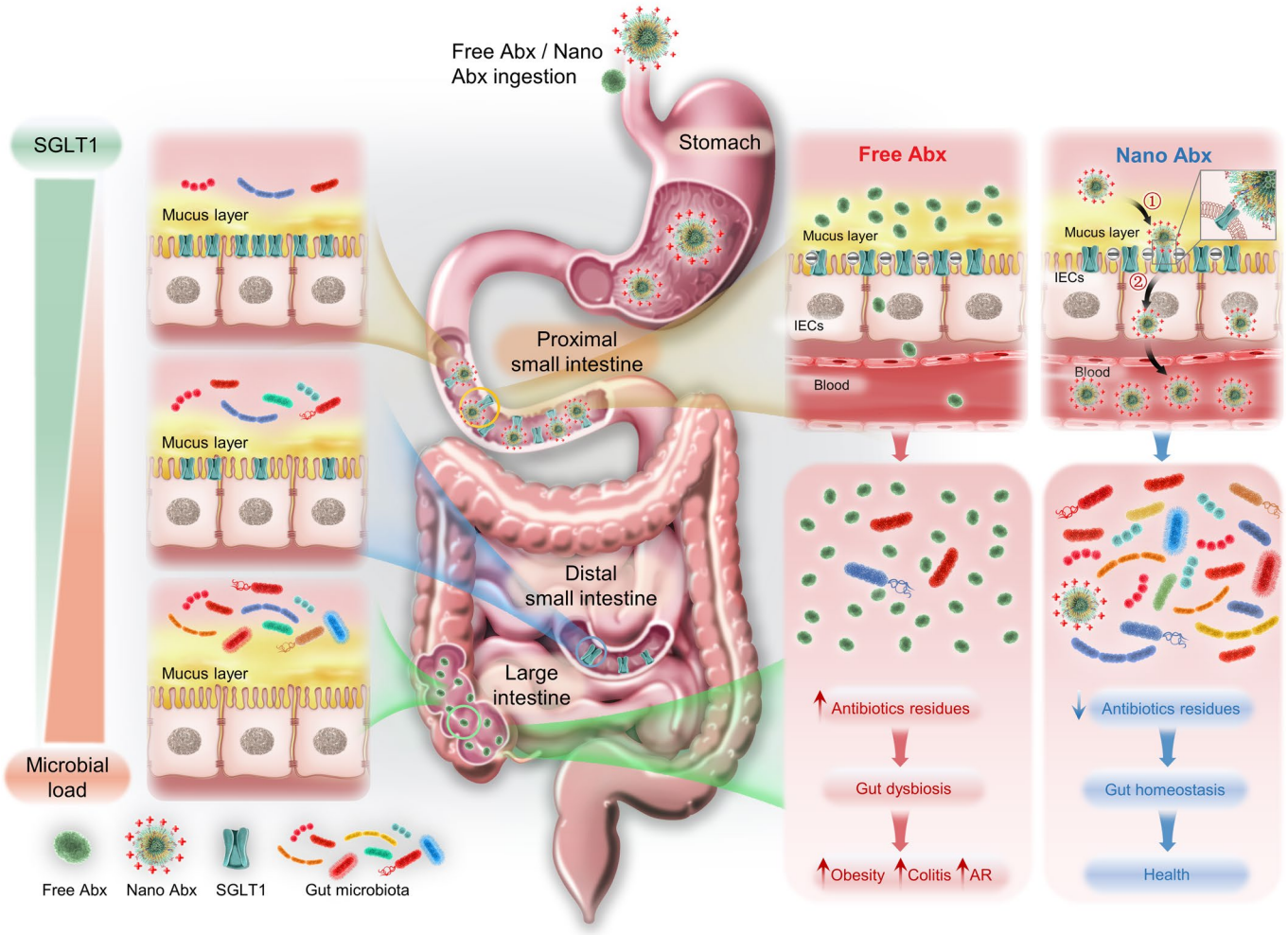

Extended Data Fig. 1 | A proposed model for how PGNPs for oral delivery of antibiotics resolve antibiotic-associated dysbiosis. The different segments of the intestine have quite distinct appearances. Distribution of gut microbiota is increasing along the length of the intestine while the expression of glucose transporter SGLT1 along small intestine is decreasing and no detection in large intestine. When oral free antibiotics to cure bacterial infection induced damages to the gut microbiota and related adverse effects in normal mice. But, when oral nanocarrier antibiotics alleviates disruptions to the gut microbiota and keep it homeostasis.

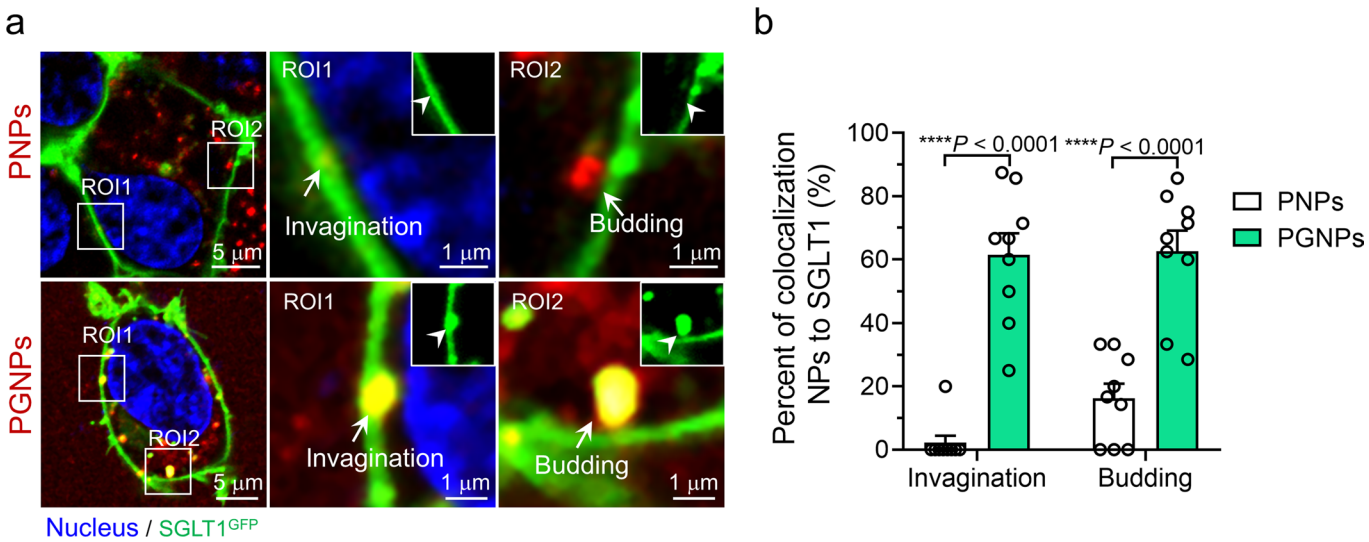

Extended Data Fig. 2 | SGLT1 aids the uptake of PGNPs into cells. a, Representative confocal images showing SGLT1-mediated endocytosis of PGNPs in SGLT1-expressing HEK293T cells. PNPs or PGNPs (red), SGLT1 (green), and nucleus (blue). Scale bars, 5 μm (left panel), 1 μm (middle and right panels). **b**, Quantification of the percentage of PNPs or PGNPs co-localized with SGLT1 during the internalization in confocal images. $n = 3$. All values are expressed as mean ± s.e.m. Statistical significance was determined using two-tailed Student's t-test in **b**. $^{*}P < 0.05$, $^{**}P < 0.01$, $^{***}P < 0.001$, $^{****}P < 0.0001$. **a** and **b** are representative of two independent experiments.

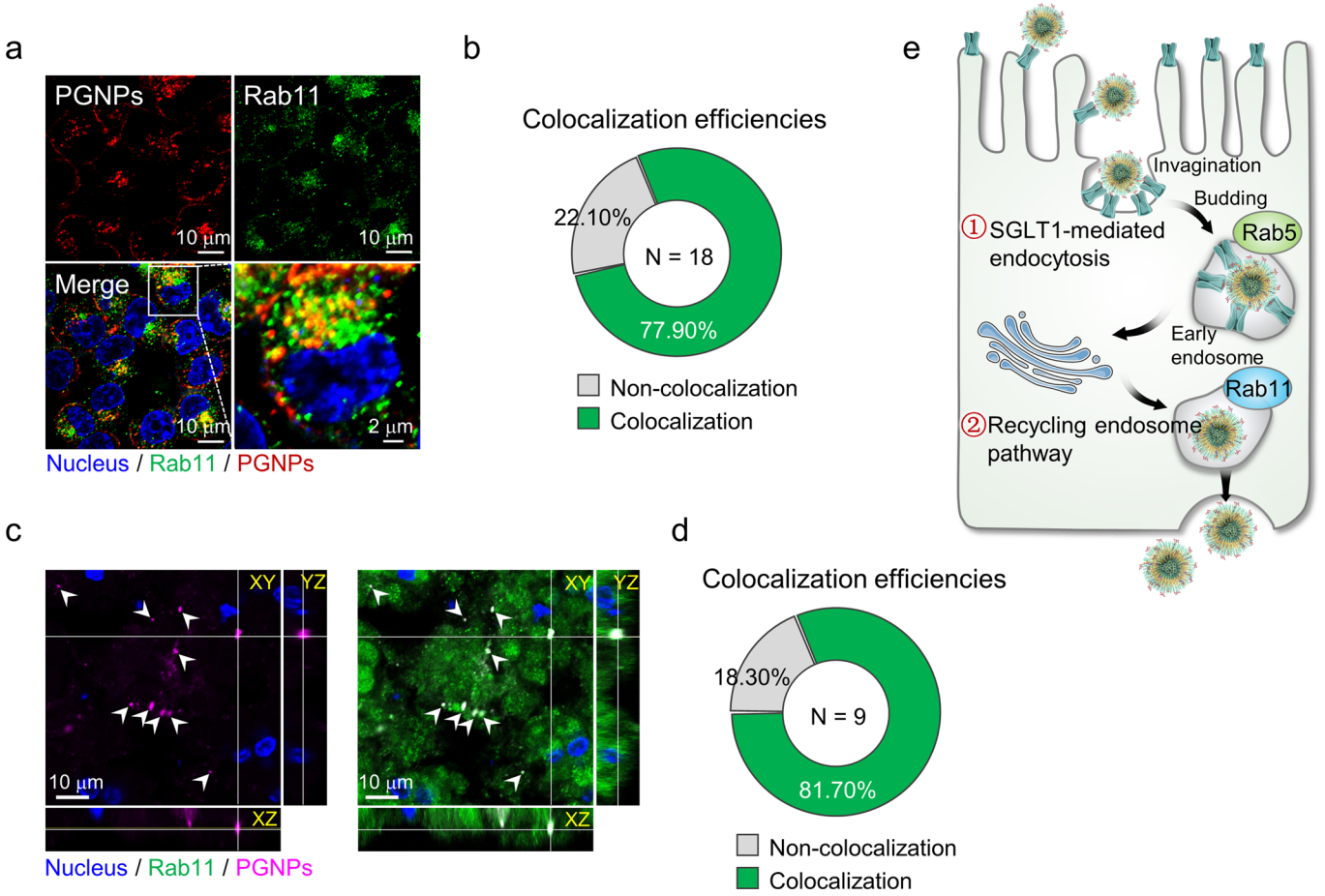

Extended Data Fig. 3 | PGNPs co-localized with recycling endosome. a, Representative confocal images showing the co-localization of PGNPs-DiD with Rab11 in SGLT1-expressing HEK293T cells. PGNPs-DiD (red), Rab11 (green), nucleus (blue). Scale bars, 10 μm. **b**, The percentage of co-localized PGNPs-DiD and Rab11 was quantified in (**a**). $n = 18$ images from three biologically independent samples. **c**, Representative confocal images showing the co-localization of PGNPs with Rab11 in proximal small intestine. PGNPs-DiD (purple), Rab11 (green), and nucleus (blue). Scale bars, 10 μm. **d**, The percentage of co-localized PGNPs-DiD and Rab11 was quantified in (**c**). $n = 9$ images from three mice. **e**, Schematic representation showing that PGNPs can be taken up and transported through SGLT1-mediated endocytosis and transcytosis in intestinal epithelial cells. All values are expressed as mean ± s.e.m. **a**–**d** are representative of two independent experiments.

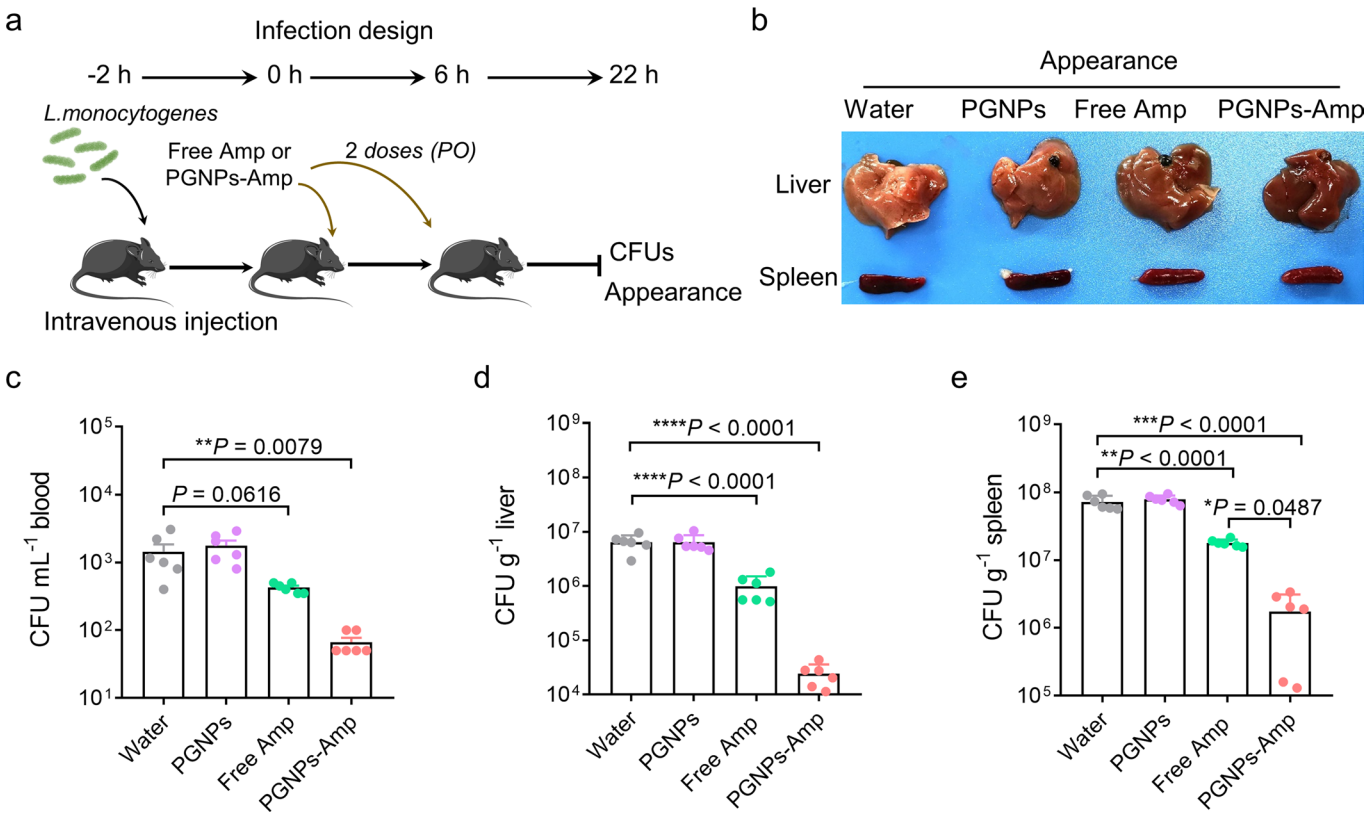

Extended Data Fig. 4 | PGNPs-Amp effectively eliminate *Listeria monocytogenes* in a bacteremia model. a, Study design: mice were received an intravenous injection with 2×10^6 CFUs of *Listeria monocytogenes*. Free Amp (40 mg kg^{-1}) or Amp (40 mg kg^{-1})-loaded PGNPs was orally administered into mice. Control mice did not receive antibiotic treatment. Bacterial loads in blood, liver, spleen were determined at 24 h post infection. **b**, The appearance of the infected liver and spleen in mice with indicated treatments at 24 h post infection. **c**–**e**, Quantification of bacteria CFUs in the blood (**c**), liver (**d**), and spleen (**e**) at 24 h post infection. $n = 6$ mice. All values are expressed as mean ± s.e.m. Statistical significance was determined using one-way ANOVA with Tukey's multiple comparisons test in (**c**, **d** and **e**). $^*P < 0.05$, $^{**}P < 0.01$, $^{***}P < 0.001$, $^{****}P < 0.0001$. **b**–**e** are representative of two independent experiments.

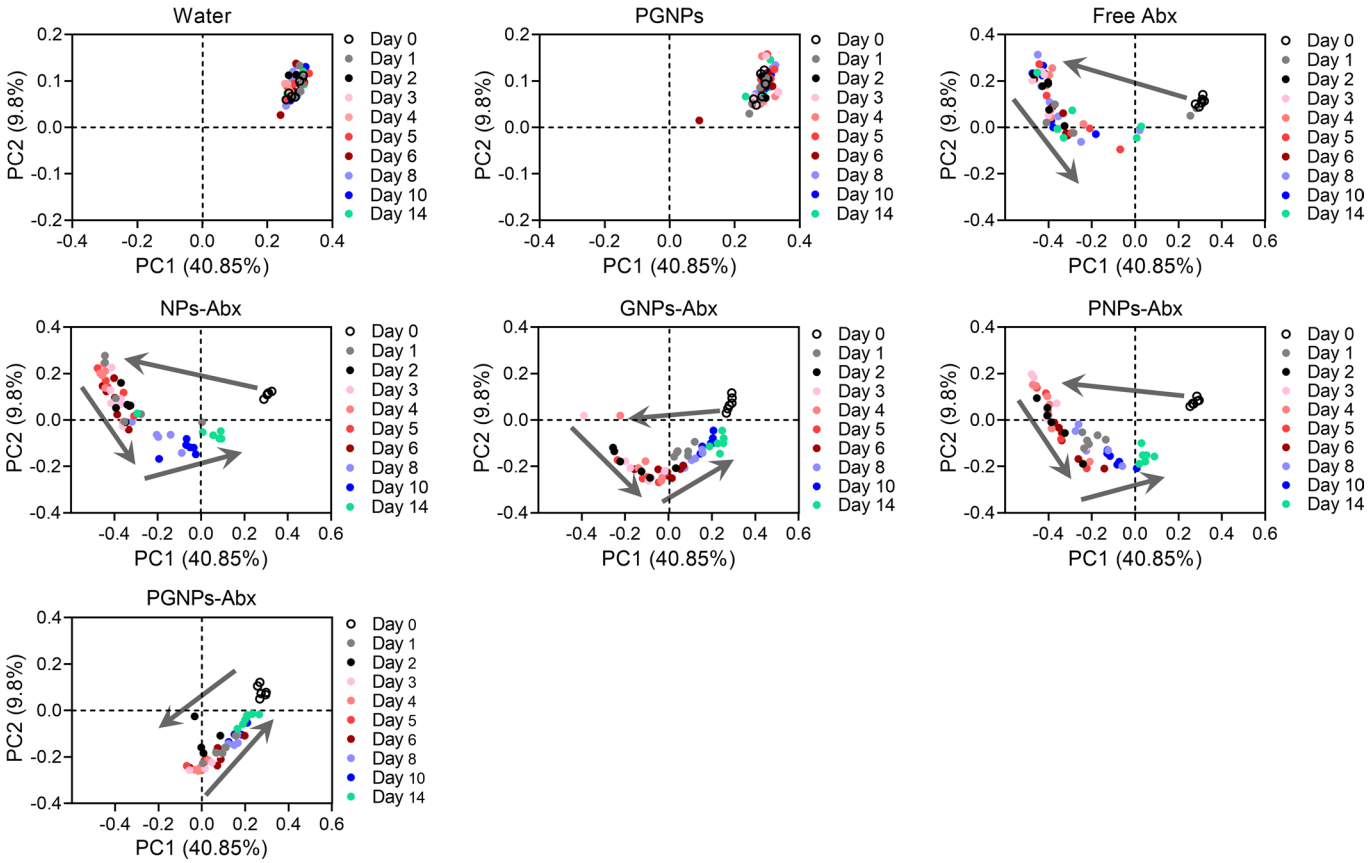

Extended Data Fig. 5 | PGNPs delivery of antibiotics show minimized alteration of the microbiota. PCoA analysis of microbiota community composition in mice treated with free Abx or Abx-loaded NPs and the recovery trajectory are marked by analyzing unweighted UniFrac distances.

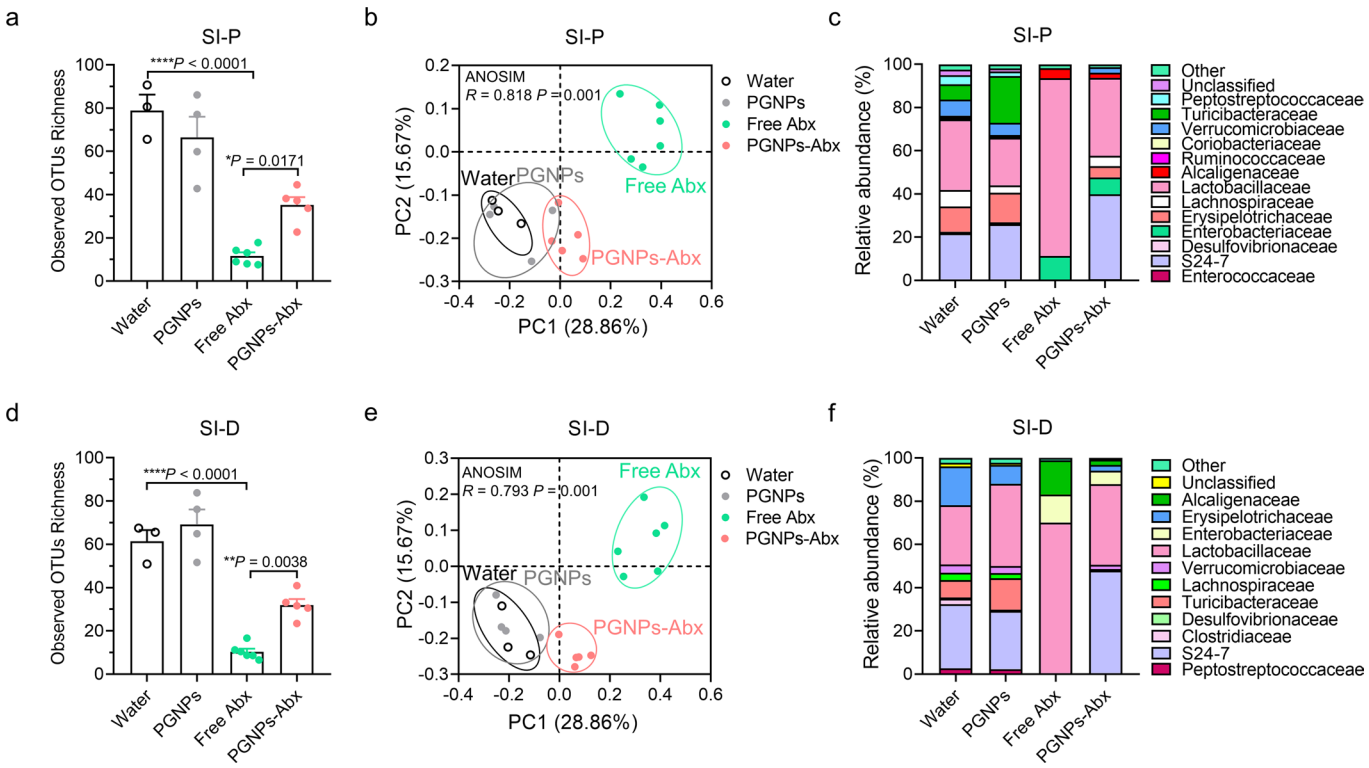

Extended Data Fig. 6 | PGNPs delivery of antibiotics reduces the microbiota alteration in small intestine. C57BL/6 mice were orally administered with free or ampicillin (20 mg kg^{-1}) and vancomycin (20 mg kg^{-1})-loaded PGNPs for 5d. Control mice had no antibiotic exposure. Both SI-P and SI-D content were collected for 16 s rRNA sequencing at the end of treatment. **a**,**d**, Alpha diversity quantified as observed species in SI-P (**a**) or SI-D (**d**) in indicated groups. **b**,**e**, Unweighted UniFrac principal-coordinates analysis (PCoA) of samples with indicated treatments in SI-P (**b**) and SI-D (**e**). **c**,**f**, Relative abundance of family-level taxonomy in fecal microbiota was presented as a percentage of the total detected sequences in SI-P (**c**) and SI-D (**f**). $n \geq 3$ mice. All values are expressed as mean ± s.e.m. Statistical significance was determined using one-way ANOVA with Tukey's multiple comparisons test in **a** and **d**. $^{*}P < 0.05$, $^{**}P < 0.01$, $^{***}P < 0.001$, $^{****}P < 0.0001$.

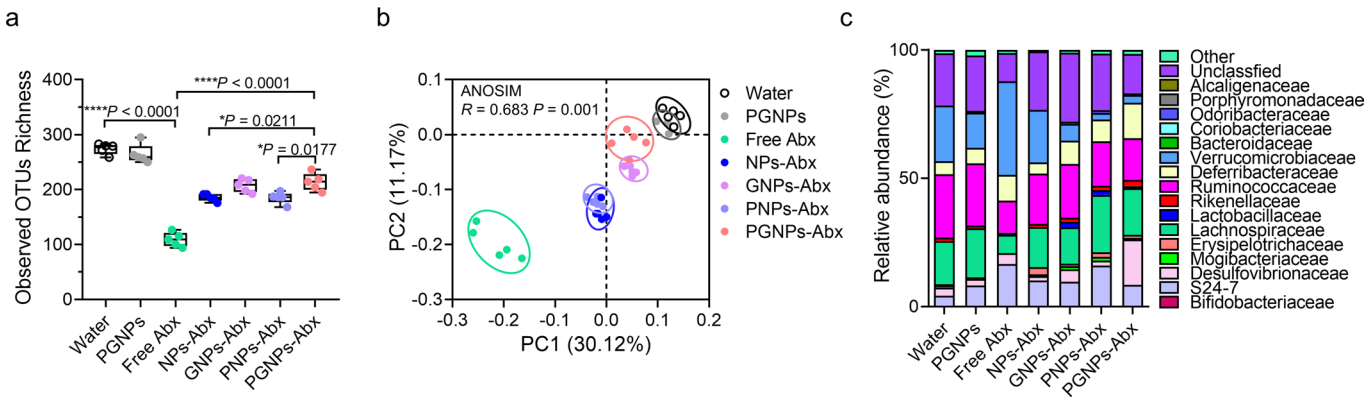

Extended Data Fig. 7 | Microbiota alterations upon Antibiotics (Abx) and HFD treatments. Three-week-old C57BL/6 J male mice were administrated with free antibiotics or ampicillin (20 mg kg^{-1}) and vancomycin (20 mg kg^{-1})-loaded nanoparticles for 5 successive days. Control mice had no antibiotics exposure. All mice were treated with HFD from age of 7 weeks. Fecal pellets were collected on the day end of the HFD treatment for 16S rRNA sequencing. **a**, The observed species number of gut microbiota. **b**, PCA plot generated from unweighted UniFrac distance matrix displaying the distinct clustering pattern of gut microbiota. **c**, Relative abundances of the gut commensal microorganisms at the family level. $n = 5$ mice. All values are expressed as the mean ± s.e.m. Statistical significance was determined using one-way ANOVA with Tukey's multiple comparisons test in **a**. $^{*}P < 0.05$, $^{**}P < 0.01$, $^{***}P < 0.001$, $^{****}P < 0.0001$.

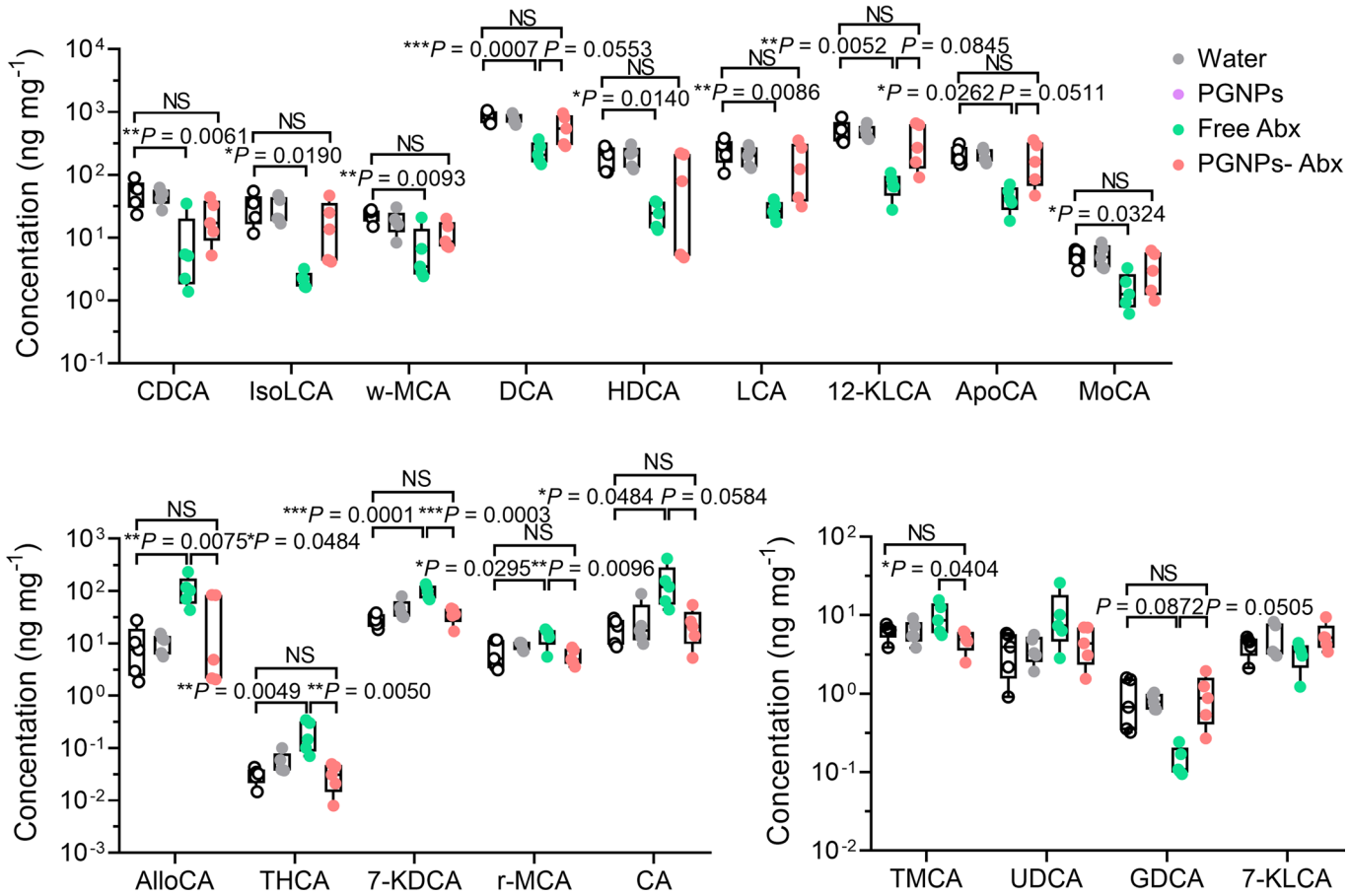

Extended Data Fig. 8 | Fecal bile acids levels after short-time antibiotics treatment following with a high-fat diet exposure. Bile acids levels altered by free Abx or PGNPs-Abx were analyzed by mass spectrometer. $n = 5$ mice. All values are expressed as mean ± s.e.m. Statistical significance was determined using one-way ANOVA with Tukey's multiple comparisons. $^{*}P < 0.05$, $^{**}P < 0.01$, $^{***}P < 0.001$, $^{****}P < 0.0001$. NS, no significance.

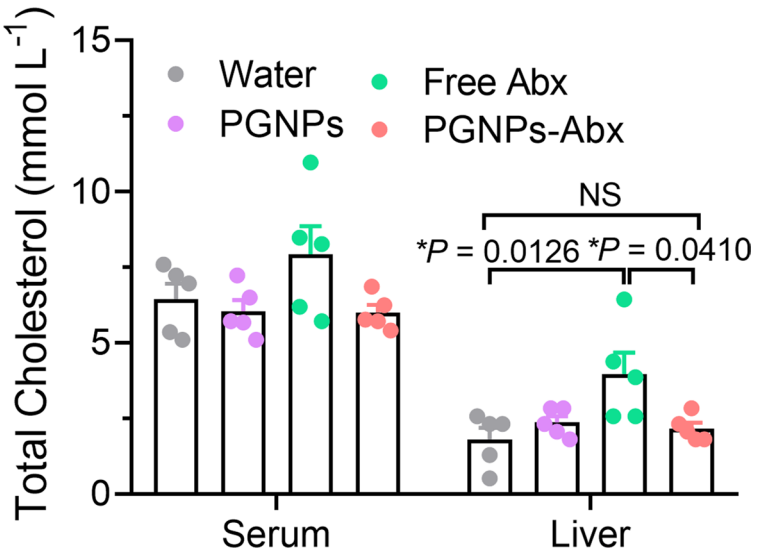

Extended Data Fig. 9 | Fecal microbiota transplantation (FMT) from free Abx- but not PGNPs-Abx- treated mice results in metabolic alteration. Donor mice were given Water, PGNPs, free Abx, or PGNPs-Abx daily for 5 days. Fecal pellets were collected for FMT. Fecal bacteria were transplanted into recipient mice after Abx treatment and followed by HFD feeding to induce obesity. Serum and liver cholesterol levels were measured after 13 weeks HFD. $n = 5$ mice. All values are expressed as mean ± s.e.m. Statistical significance was determined using one-way ANOVA with Tukey's multiple comparisons. $^{*}P < 0.05$, $^{**}P < 0.01$, $^{***}P < 0.001$, $^{****}P < 0.0001$. NS, no significance. Data is representative of two independent experiments.

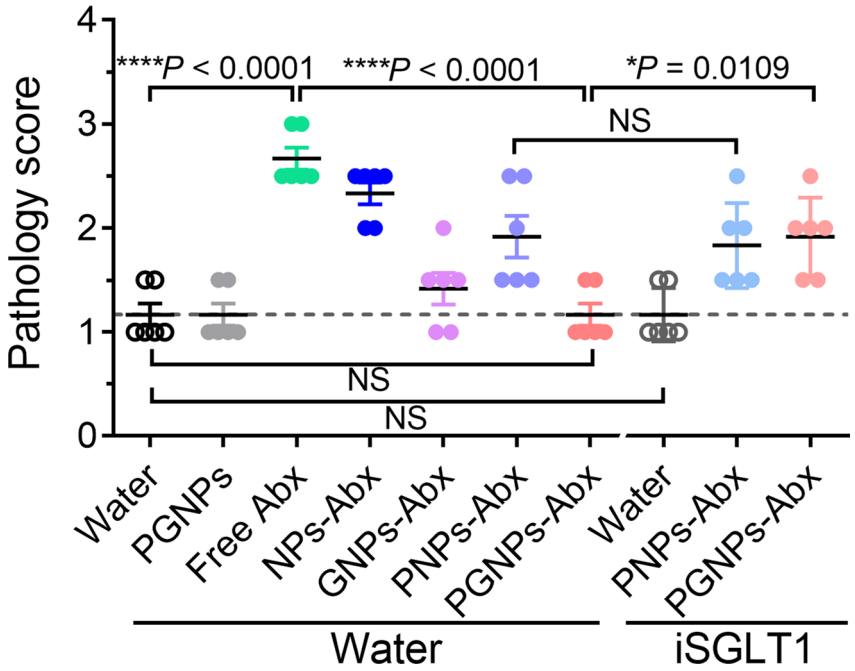

Extended Data Fig. 10 | Quantification of pathological scores of cecum sections from the *C. rodentium* infected mice. $n = 6$ mice. All values are expressed as mean ± s.e.m. Statistical significance was determined using one-way ANOVA with Tukey's multiple comparisons. $^{*}P < 0.05$, $^{**}P < 0.01$, $^{***}P < 0.001$, $^{****}P < 0.0001$. NS, no significance.

nature portfolio

Corresponding author(s): Yucai Wang and Shu Zhu

Last updated by author(s): May 14, 2022

Reporting Summary

Nature Portfolio wishes to improve the reproducibility of the work that we publish. This form provides structure for consistency and transparency in reporting. For further information on Nature Portfolio policies, see our Editorial Policies and the Editorial Policy Checklist.

Statistics

For all statistical analyses, confirm that the following items are present in the figure legend, table legend, main text, or Methods section.

n/a	Confirmed
☐	☒ The exact sample size (*n*) for each experimental group/condition, given as a discrete number and unit of measurement
☐	☒ A statement on whether measurements were taken from distinct samples or whether the same sample was measured repeatedly
☐	☒ The statistical test(s) used AND whether they are one- or two-sided *Only common tests should be described solely by name; describe more complex techniques in the Methods section.*
☒	☐ A description of all covariates tested
☒	☐ A description of any assumptions or corrections, such as tests of normality and adjustment for multiple comparisons
☐	☒ A full description of the statistical parameters including central tendency (e.g. means) or other basic estimates (e.g. regression coefficient) AND variation (e.g. standard deviation) or associated estimates of uncertainty (e.g. confidence intervals)
☐	☒ For null hypothesis testing, the test statistic (e.g. *F*, *t*, *r*) with confidence intervals, effect sizes, degrees of freedom and *P* value noted *Give P values as exact values whenever suitable.*
☒	☐ For Bayesian analysis, information on the choice of priors and Markov chain Monte Carlo settings
☒	☐ For hierarchical and complex designs, identification of the appropriate level for tests and full reporting of outcomes
☒	☐ Estimates of effect sizes (e.g. Cohen's *d*, Pearson's *r*), indicating how they were calculated

Our web collection on statistics for biologists contains articles on many of the points above.

Software and code

Policy information about availability of computer code

Data collection

IVIS images: IVIS spectrum (Perkin Elmer)
Flow-cytometric data: CytoFLEX (BECKMAN), FACSverse (BD Biosciences)
Fluorescent images were acquired with confocal laser scanning microscope (CLSM, Nikon, Tokyo, Japan)
HE images were acquired with light microscope (TissueFAXS PLUS)
Real-time assays: CFX384 Touch Real-Time PCR Detection System (BIO-RAD)
16S rRNA gene sequencing: MiSeq (Illumina)
RNAseq: Novaseq 6000 system (Illumina)
Metagenomic sequencing: Novaseq 6000 system (Illumina)
Isolated resistant-bacteria: Electrotek anaerobic workstations
DLS/zeta: (Zetasizer Nano ZS90)
The morphologies of NPs: transmission electron microscope (TEM; JEOL2010, Tokyo, Japan)

Data analysis	Statistical analysis: GraphPad Prism (ver. 8) IVIS analysis: Tissue FAXS Viewer software (Tissue Gnostics) Fuorescent and HE images were analyzed using Image J software Flow cytometric analysis: FlowJo (Version7.6.1 for Windows) Real-time analysis: BioRad CFX Manager (version 3.1) Microbial diversity was analyzed by usearch (v8.1), vsearch (v2.13.0)and QIIME (v1.9.1), ANOSIM analyses were performed with the vegan package (v2.5-7) in R (v4.0.5) Raw RNA-sequencing reads were aligned to the mouse genome (mm10, GRCm38) with STAR(v2.5.3a). Raw Metagenomic reads were assembled and processed by Megahit (V1.2.9),CD-hit (v4.8.1) and Prodigal (V2.6.3). Then antimicrobial resistance genes were screened agaist CARD database by Abricate(V1.0.1) and quantified by Salmon (v1.5.1)

For manuscripts utilizing custom algorithms or software that are central to the research but not yet described in published literature, software must be made available to editors and reviewers. We strongly encourage code deposition in a community repository (e.g. GitHub). See the Nature Portfolio guidelines for submitting code & software for further information.

Data

Policy information about availability of data

All manuscripts must include a data availability statement. This statement should provide the following information, where applicable:

- Accession codes, unique identifiers, or web links for publicly available datasets
- A description of any restrictions on data availability
- For clinical datasets or third party data, please ensure that the statement adheres to our policy

The main data supporting the results in this study are available within the paper and its Supplementary Information. All sequence data generated in this study are available from the SRA database with accession numbers PRJNA666621 and PRJNA666612. Source data are provided with this paper.

Field-specific reporting

Please select the one below that is the best fit for your research. If you are not sure, read the appropriate sections before making your selection.

☒ Life sciences ☐ Behavioural & social sciences ☐ Ecological, evolutionary & environmental sciences

For a reference copy of the document with all sections, see nature.com/documents/nr-reporting-summary-flat.pdf

Life sciences study design

All studies must disclose on these points even when the disclosure is negative.

Sample size	Sample sizes for the animal experiments were estimated on the basis of our prior experience of performing similar sets of experiments. We mostly chose sample sizes of 3–6 for the in vitro and in vivo experiments, on the basis of standard practices in the field.
Data exclusions	No data were excluded from the analyses.
Replication	All experiments were independently reproduced as stated in the figure legends and no problems of reproducibility were observed.
Randomization	Mice were randomly allocated to each group.
Blinding	The histological analyses were performed in a blinded manner.

Reporting for specific materials, systems and methods

We require information from authors about some types of materials, experimental systems and methods used in many studies. Here, indicate whether each material, system or method listed is relevant to your study. If you are not sure if a list item applies to your research, read the appropriate section before selecting a response.

Materials & experimental systems

n/a	Involved in the study
☐	☒ Antibodies
☐	☒ Eukaryotic cell lines
☒	☐ Palaeontology and archaeology
☐	☒ Animals and other organisms
☐	☒ Human research participants
☒	☐ Clinical data
☒	☐ Dual use research of concern

Methods

n/a	Involved in the study
☒	☐ ChIP-seq
☐	☒ Flow cytometry
☒	☐ MRI-based neuroimaging

Antibodies

Antibodies used	Dilution of each antibody used for FACS analysis is 1:100. Anti-mouse APC-Cy7-CD45.2, Biolegend, Cat#109824, Lot#B316182, Clone#104 Anti-mouse PE-CD14, Biolegend, Cat#150106, Lot#B294892, Clone#M14-23 Anti-mouse PE-Cy7-CD11b, Biolegend, Cat#101216, Lot#B346888, Clone#M1/70 Anti-mouse FITC-Ly6G, Biolegend, Cat#127606, Lot#B277117, Clone#1A8 For immunofluorescence staining. Rab11a antibody (1:100, Cat#2413, Cell Signaling Technology) SGLT1 antibody (1:100, Cat#20801, BiCell Scientific) Secondary antibody (1:200, REF#A11071, Lot#2309137)
Validation	Anti-mouse APC-Cy7-CD45.2, Biolegend, Cat#109824, Lot#B316182, Clone#104. Validation stated on supplier's website: https://www.biolegend.com/en-us/products/apc-cyanine7-anti-mouse-cd45-2-antibody-3906. Anti-mouse PE-CD14, Biolegend, Cat#150106, Lot#B294892, Clone#M14-23. Validation stated on supplier's website: https://www.biolegend.com/en-us/products/pe-anti-mouse-cd14-antibody-15675?GroupID=GROUP20. Anti-mouse PE-Cy7-CD11b, Biolegend, Cat#101216, Lot#B346888, Clone#M1/70. Validation stated on supplier's website: https://www.biolegend.com/en-us/products/pe-cyanine7-anti-mouse-human-cd11b-antibody-1921?GroupID=BLG10427. Anti-mouse FITC-Ly6G, Biolegend, Cat#127606, Lot#B277117, Clone#1A8. Validation stated on supplier's website: https://www.biolegend.com/en-us/products/fitc-anti-mouse-ly-6g-antibody-4775?GroupID=BLG5803. Rab11a antibody (Cat#2413, Cell Signaling Technology). Validation stated on supplier's website: https://www.cellsignal.com/products/primary-antibodies/rab11a-antibody/2413. SGLT1 antibody (Cat#20801, BiCell Scientific).Validation stated on supplier's website: https://bicellscientific.com/product/sglt1-human-antibody/. Secondary antibody (1:200, REF#A11071, Lot#2309137). Validation stated on supplier's website: https://www.thermofisher.cn/cn/zh/antibody/product/Goat-anti-Rabbit-IgG-H-L-Cross-Adsorbed-Secondary-Antibody-Polyclonal/A-11071.

Eukaryotic cell lines

Policy information about cell lines

Cell line source(s)	HEK293T (ATCC CRL-3216), obtained from the American Type Culture Collection (ATCC).
Authentication	All cell lines were authenticated on the basis of their morphology and growth condition.
Mycoplasma contamination	The cells were not tested for mycoplasma contamination.
Commonly misidentified lines (See ICLAC register)	No commonly misidentified cell lines were used.

Animals and other organisms

Policy information about studies involving animals; ARRIVE guidelines recommended for reporting animal research

Laboratory animals	C57BL/6 mice were purchased from GenPharmatech (Nanjing, China). Mice aged 3–10 weeks were used. Animals were maintained at 21±1°C, in 40% to70% humidity, and with a 12 hours light/dark cycle (from 8 a.m. to 8 p.m.)
Wild animals	The study did not involve wild animals.
Field-collected samples	The study did not involve samples collected from the field.
Ethics oversight	All animal studies were approved by the institutional review board at University of Science and Technology of China (USTCACUC202101046).

Note that full information on the approval of the study protocol must also be provided in the manuscript.

Human research participants

Policy information about studies involving human research participants

Population characteristics	Intestinal specimens from human donors (n = 9) were collected at the First Affiliated Hospital of Anhui Medical University (Hefei, China). All patients provided written informed consent.
Recruitment	Biopsies were obtained from the intestine of nine individuals undergoing screening enteroscopy. Participation was voluntary.
Ethics oversight	All human samples used in the present study were obtained under the approval of the Ethics Committee of The First Affiliated Hospital of University of Science and Technology of China (2021KY02).

Note that full information on the approval of the study protocol must also be provided in the manuscript.

Flow Cytometry

Plots

Confirm that:

☒ The axis labels state the marker and fluorochrome used (e.g. CD4-FITC).

☒ The axis scales are clearly visible. Include numbers along axes only for bottom left plot of group (a 'group' is an analysis of identical markers).

☒ All plots are contour plots with outliers or pseudocolor plots.

☒ A numerical value for number of cells or percentage (with statistics) is provided.

Methodology

Sample preparation	The lungs were collected, and tissue passed through a 200-gauge mesh. The supernatants were centrifuged at 500 g for 5 min. The cell pellet was further treated with 2 mL Red Cell Lysing Buffer (Biosharp, Cat#BL503A) to remove red blood cells for 5 min at 4 °C in 15-mL conical. Cell pellets were re-suspended for further surface staining for flow analysis.
Instrument	CytoFLEX (BECKMAN), FACSverse (BD Biosciences)
Software	FlowJo (Version7.6.1 for Windows)
Cell population abundance	No sorting was performed by flow cytometry.
Gating strategy	For all experiments, cells were first gated by FSC/SSC to exclude debris, followed by gating FSC-A and FSC-H to eliminate non-singlets. Then, target cell population for further analysis were gated by cell surface marker.

☒ Tick this box to confirm that a figure exemplifying the gating strategy is provided in the Supplementary Information.